ABSTRACT

A MEASUREMENT OF THE DIFFERENTIAL CROSS SECTIONS

FOR THE REACTIONS

$\pi^+ + p \rightarrow K^+ + \Sigma^+$ AND $\pi^+ + p \rightarrow K^+ + Y^{*+}(1385)$

NEAR ZERO DEGREES

AT 3.0, 5.0 AND 7.0 Gev/c

by

Parviz Kalbaci

Chairman: C. Tristram Coffin

The differential cross sections for the reactions $\pi p \rightarrow K^+\Sigma^+$ and $\pi^+ p \rightarrow K^+ Y^{*+}$ have been measured for kaon laboratory angles from 0° to 3.5°. A single-arm, missing-mass spectrometer determined the direction and momentum of forward going kaons. The spectrometer consisted of bending magnets, scintillation counters, gas threshold Cerenkov counters and wire spark chambers connected to an on-line computer.

The differential cross sections for $\pi p \rightarrow K^+\Sigma^+$ rise exponentially to t_{min} at 5.0 and 7.0 Gev/c. However, the cross section at 3.0 Gev/c deviates from a simple exponential shape indicating a possibility of an s-channel contribution to the cross section. There is no evidence of a dip at very small -t indicating that the spin flip contribution to the cross sections for this reaction is small.

The results at high energies are compatible with double Regge pole models in the forward direction.

The reaction $\pi p \rightarrow K^+ Y^*$ shows a sharp dip at very small -t indicating the dominance of the spin flip contribution to the cross section. The 'ρ-photon analogy' has been employed to interpret this forward dip.

UM HE 71-41

A MEASUREMENT OF THE DIFFERENTIAL CROSS SECTIONS FOR THE REACTIONS $\pi^+ + p \rightarrow K^+ + \Sigma^+$ AND $\pi^+ + p \rightarrow K^+ + Y^{*+}(1385)$ NEAR ZERO DEGREES AT 3.0, 5.0 AND 7.0 Gev/c

by

Parviz Kalbaci

A dissertation submitted in partial fulfillment
of the requirements for the degree of
Doctor of Philosophy
(Physics)
in The University of Michigan
1971

Doctoral Committee:

Associate Professor C. Tristram Coffin, Chairman
Professor Wilfred Kaplan
Professor Donald I. Meyer
Assistant Professor Brian E. Springett
Associate Professor Yukio Tomozawa

ACKNOWLEDGEMENTS

I wish to thank Professor C. Tristram Coffin for his calm, patient advice and encouragement at all stages of my thesis work. I would like to thank Professor Donald I. Meyer for his many helpful suggestions and continuous assistance throughout the experiment. I am indebted to Professor Carl W. Akerlof for his invaluable contributions and guidance during the experiment and also for his perceptive comments on my thesis work. Thanks are due to Dr. Kenneth C. Stanfield for his assistance from the very beginning to the final data analysis. I would like to express my gratitude to Dr. Peter Schmueser for both his advice and building of most of the spark chambers. I appreciate the assistance of Dr. Paul K. Caldwell in running the experiment.

I would like to thank Professors Yukio Tomozawa and Gordon L. Kane for helpful discussions. I would also like to extend my thanks to Professors Wilfred Kaplan and Brian E. Springett.

I wish to thank Dr. David R. Rust, particularly for building the high voltage pulser. Finally, acknowledgement is extended to the staff of the Argonne National Laboratory.

TABLE OF CONTENTS

LIST OF TABLES

LIST OF FIGURES

LIST of FIGURES (cont'd)

LIST OF APPENDICES

I. INTRODUCTION

The strong interactions are responsible for such processes as the scattering of mesons by baryons, of baryons by baryons and for the forces that bind protons and neutrons together in the nucleus. Much of our knowledge of strong interactions comes from the two-body reactions of the form

$$a + b \rightarrow c + d$$

The most successful theories for such reactions are based on the concept of particle exchange.[1] Figure 1 shows the Feynman diagram for a two-body reaction mediated by the exchange of one particle.

The behavior of the two-body reactions has been found to depend on the quantum numbers exchanged between the interacting particles. If the exchanged quantum numbers are such that a particle with these quantum numbers exists, the cross section for the corresponding reaction is large; otherwise it is relatively small. For instance, the reaction $K^- + p \rightarrow \pi^- + \Sigma^+$ requires a meson exchange with quantum numbers $I=1/2$, $S=-1$ and $Q=0$. Since there exist meson resonances with these quantum numbers such as $K^*(m=890, J^p=1^-, I=1/2, S=-1)$ and $K^{**}(m=1420, J^p=2^+, I=1/2, S=-1)$, one expects a forward peak in the cross section and it is observed.[2] However, the reaction $K^- + p \rightarrow \pi^+ + \Sigma^-$

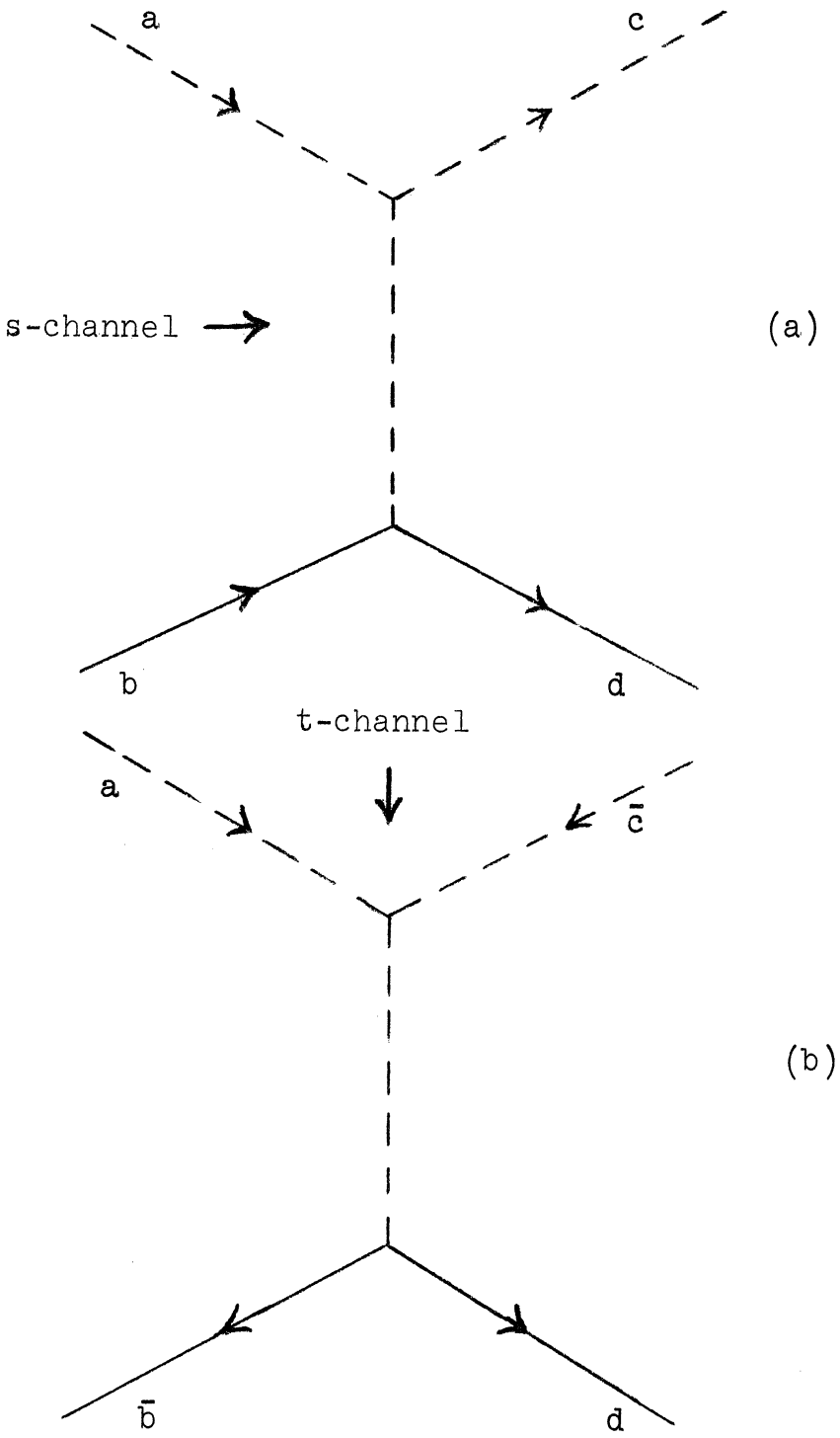

Figure 1. The Feynman diagram of two-body reactions a) a + b → c + d as viewed from s-channel. b) a + $\bar{c}$ → $\bar{b}$ + d as viewed from t-channel.

in the forward direction requires the exchange of a meson with I=3/2, S=1 and Q=2. Since there are no doubly charged mesons, the forward cross section should be much smaller than the forward cross section for $K^- + p \rightarrow \pi^- + \Sigma^+$ and it is.[2,3]

Before proceeding further with examples of relationship between cross section and quantum numbers exchanged, it is convenient to define some kinematic variables. The two-body reactions are described by two independent Lorentz invariant variables. The most common variables used are the Mandelstam variables s and t which are defined as follows:

$$s=-(p_a + p_b)^2=E^{*2}$$

$$t=-(p_a - p_c)^2$$

Where p's are the four momenta of the corresponding particles, $p(\vec{p},iE)$. E^* is the energy in the center-of-mass system and t is the square of the four momentum transfer from a to c.

The following set of reactions illustrates the relationship between the structure of the cross section and the quantum numbers of the exchanged particles.

$$\pi^- + p \rightarrow \pi^- + p \qquad (1)$$

$$\pi^+ + p \rightarrow \pi^+ + p \qquad (2)$$

$$\pi^- + p \rightarrow \pi^o + n \qquad (3)$$

$$\pi^- + p \rightarrow \eta^o + n \qquad (4)$$

The dominant exchanges of the quantum numbers for the elastic scattering reactions (1) and (2) are the quantum numbers of the vacuum (B=I=S=0), or the pomeranchuck trajectory in the language of the Regge pole theory.[4] However, the leading trajectories for the charge exchange reactions (3) and (4)

are the ρ and A_2 trajectories respectively. Figure 2 demonstrates the structure of the measured cross section for some of the two-body reactions with different exchanges. The differential cross sections for the elastic scattering (1) and (2) are measured at different incident pion energies, for pions production at different angles in the final states, by many authors.[5,6] The general features of these two reactions are the exponential decrease of the cross section as a function of t followed by a second maximum as shown in Figure 2 (a and b). The second maximum starts to disapear as the incident pion energy increases. The charge exchange reactions, (3) and (4), show a peak in the small momentum transfer.[7-9] Such a peak is not steeply decreasing from the forward direction, as is the elastic peak, but rather it is flat up to $-t \simeq .1$ $(\text{Gev/c})^2$ and then decreases exponentially with a slope $b \simeq 10$ $(\text{Gev/c})^{-2}$ for the reaction (3) and a slope $b \simeq 4$ $(\text{Gev/c})^{-2}$ for the reaction (4). Figure 2 (c and d) shows the behavior of the cross section for the reactions (3) and (4). The study of the reactions 1 through 4 has provided information for determining the corresponding exchanged trajectories.

Another class of reactions of interest comprises the hypercharge exchange reactions. The following processes are of special interest because they are convenient to study experimentally.

$$\pi^+ + p \rightarrow K^+ + \Sigma^+ \qquad (5)$$

$$\pi^+ + p \rightarrow K^+ + Y^*(1385) \qquad (6)$$

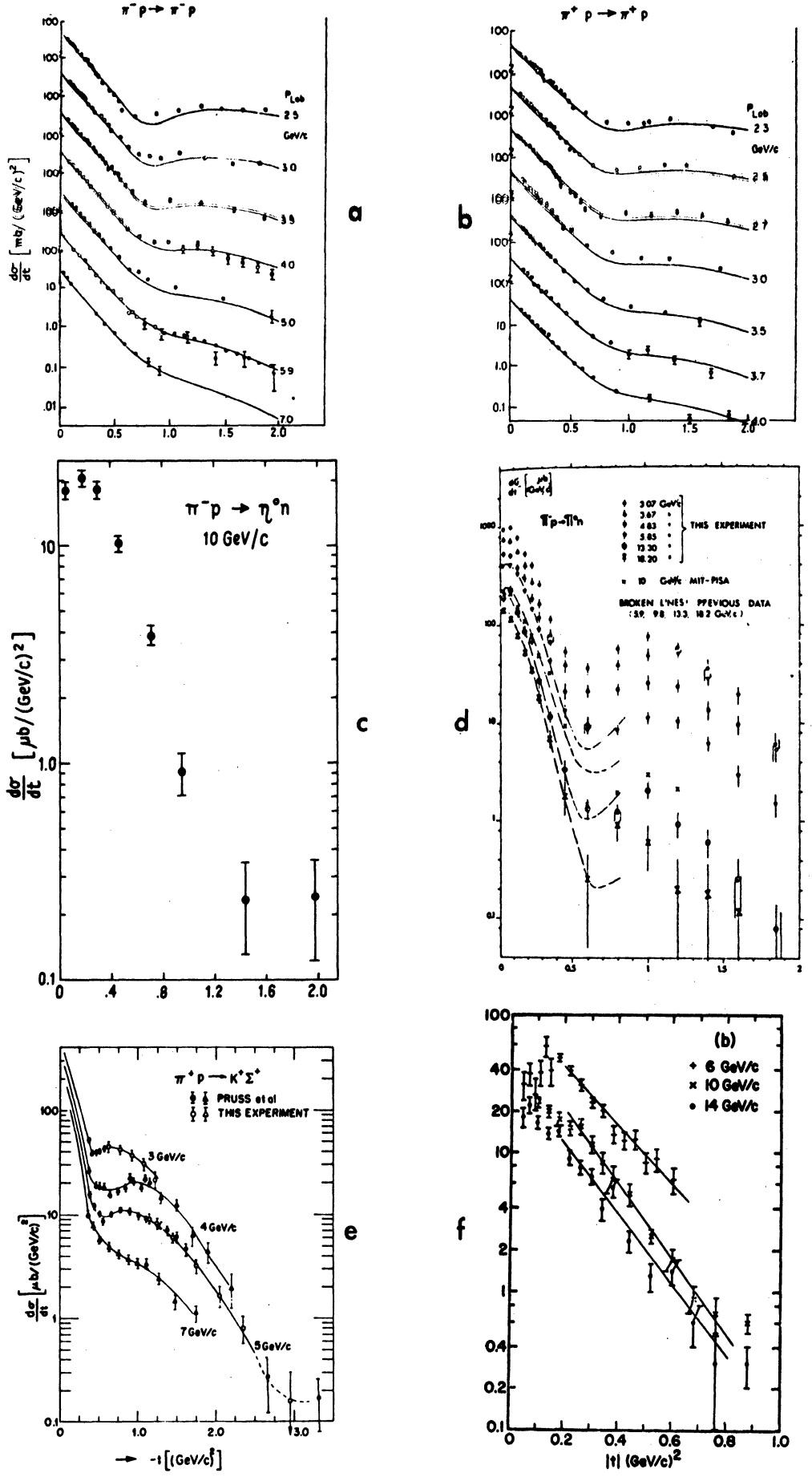

Figure 2. The differential cross section for some of the two-body reactions.

The exchanged trajectories for both these reactions are $K^{*}(890)$ and $K^{**}(1420)$. The differential cross section for reaction (5) has been measured for pion energies from 3 Gev/c to 14 Gev/c.[10-12] The cross section for this reaction shows an exponential decrease with t followed by a secondary maximum similar to the one for the charge exchange reaction (3). Figure 2 (e) shows the dependance of the cross section for reaction (5) on t and on beam momentum. The cross section for reaction (6) falls off exponentially with t and it has a dip in the forward direction.[12,13] Figure 2 (f) shows the general features of the reaction (6).

None of the above mentioned authors[10-12] have measured the cross section for the reaction (5) near zero degrees to demonstrate whether the cross section rises exponentially to t_{min}(minimum) or whether it is flat (or perhaps even dips) as in the charge exchange reaction. The dip in the forward direction in the reactions (3), (4) and (6) is due to the dominance of the spin flip amplitude, which goes to zero at zero degrees.[14]

This thesis describes an experiment which was performed to measure the differential cross section for the reactions (5) and (6) for laboratory kaon angles from 0° to 3.5°. The incident pion energies were 3.0, 5.0 and 7.0 Gev/c for reaction (5) and 5.0 Gev/c for reaction (6). One of the motivations for doing this experiment was to study the relative amount of spin flip and spin non-flip amplitudes

in the reactions (5) and (6). Another objective was to provide more detailed information on the $K^{*}(890)$ and $K^{**}(1420)$ exchanges through a study of the energy and angle dependence of the cross section.

Section II will describe the apparatus used in this experiment such as wire spark chambers, detectors, fast electronics logic, buffer system and the on-line computer. Section III will describe the method of analyzing the data. Section IV will discuss the results obtained from this experiment and compare it with other experiments. It will also discuss two theoretical models, the Regge pole and the 'ρ-photon' analogy, that are used to explain the experimental data.

II. EXPERIMENTAL METHOD

This experiment was done with a single-arm, missing-mass spectrometer to determine the direction and momentum of forward going kaons (Figure 3). The spectrometer consisted of bending magnets, scintillation counters, gas threshold Cerenkov counters and wire spark chambers with magnetostrictive readouts connected on-line to an EMR 6050 computer. The wire spark chambers were triggered on events preselected by the scintillation and Cerenkov counter system.

The identification of the $K^+\Sigma^+$ and the K^+Y^* final states among the large variety of other processes was done by calculating the mass of the final Σ or Y^*, and requiring that this mass agree within experimental uncertainity with the known masses of these particles. The mass is calculated as follows from the conservation of energy and momentum for two body reactions:

$$p_a + p_b = p_c + p_d \tag{7}$$

The missing mass can be defined as:

$$\begin{aligned}(\text{Missing mass})^2 = MM^2 = m_d^2 &= -(p_d)^2 \\ &= -(p_a + p_b - p_c)^2 \end{aligned} \tag{8}$$

In the laboratory rest frame of particle b, equation (8) reduces to:

$$MM^2 = m_a^2 + m_b^2 + m_c^2 + 2m_b\left[(m_a^2 + \vec{p}_a^{\,2})^{1/2} - (m_c^2 + \vec{p}_c^{\,2})^{1/2}\right]$$

$$-(m_a^2 + \vec{p}_a^{\,2})^{1/2}(m_c^2 + \vec{p}_c^{\,2})^{1/2} + 2|\vec{p}_a||\vec{p}_c|\cos\theta \tag{9}$$

Where $\vec{p}$'s are the three momentum of the corresponding

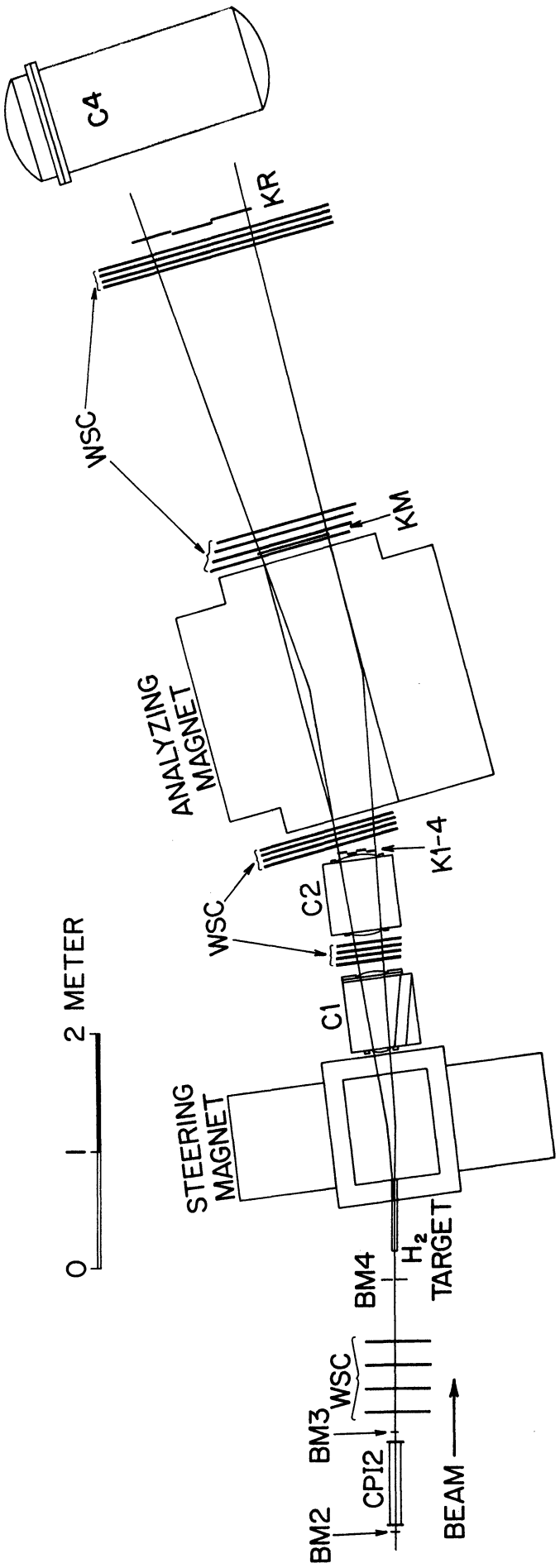

Figure 3. The experimental layout.

particle and θ is the laboratory angle between $\vec{p}_a$ and $\vec{p}_c$. Therefore for a kinematically well defined initial state, the measurement of the scattering angle and momentum of the particle c was necessary to determine MM. The wire spark chamber in the beam-line determined the direction of the incident pion beam and the spark chambers in the spectrometer determined the direction of the produced particle c in the final state. The intersection of these two direction lines defined the scattering angle. The momentum of the particle c was found from angle of bend in the analyzing magnet.

A. The Incident Beam and the Target

The extracted proton beam of the Zero Gradient Synchrotron (Z.G.S.) at Argonne National Laboratory was used to produce a secondary beam of pions from a beryllium (Be) target. These pions were focused onto a momentum slit of 3/4 in. width, by a beam transport system consisting of two quadrupoles and two bending magnets. Two scintillation counters p1 and p2, at the momentum slit, (not shown in Figure 3) were used to divide the accepted momentum into three regions. The momentum of the beam was defined to ±3/4% at the first stage of focusing. In the second stage of focusing, a set of two quadrupoles and two bending magnets recombined the momenta and focused the beam onto the hydrogen target. The characteristic parameters of the positive beam pion were

Table I.

Incident Beam Pion Parameters

Spot size	.28 in. x .22 in. RMS
Momentum spread	.63% RMS
Horizontal divergence	3.4 mrad RMS
Vertical divegence	5.3 mrad RMS
Pion intensity	$\simeq 2 \times 10^4$ per pulse
Length of the beam spill	500 msec

found by using a wire spark chamber in the beam-line. These parameters are summarized in Table I. The reason for running at low intensity was to avoid having double tracks within the resolving time (which was about .6 microseconds). The pions were tagged by two threshold gas Cerenkov counters, CPI1 and CPI2, and their positions were defined by scintillation counters BM1, BM2, BM3 and $\overline{\text{BM4}}$

The liquid hydrogen was contained in a target vessel 24 in. long and 2 in. in diameter, surrounded by a vacuum jacket 27.5 in. long, with a cross section of 5 in. inner

diameter. The H_2 was cooled by an A.D. Little Company refrigerator which reliquefied any hydrogen which boiled off the target reservoir and returned it to the target.

B. The Fast Electronics

An EVENT was defined as a coincidence between an incoming pion and an outgoing kaon produced at the hydrogen target. Figure 4 shows a flow chart of the fast logic. There were four scintillation counters BM1, BM2, BM3 and $\overline{BM4}$ to define the beam. BM1 was downstream from CPI1 and about 40 ft upstream from the hydrogen target at the first focus of the beam. BM2 and BM3 were on either end of CPI2. $\overline{BM4}$ (9 in. x 12 in.) with a square hole 3/4 in. x 3/4 in. in the middle was located immediately before the target to limit the spot size of the incident beam. The coincidence BEAM = BM1 x BM2 x BM3 x $\overline{BM4}$ indicated the number of particles entering the target. The pressures in the gas threshold Cerenkov counters, CPI1 and CPI2, were set to detect pions and not heavier particles. The coincidence, BPI = BEAM x CPI1 x CPI2, defined the pions entering the target. The only contaminations in the BPI were muons and positrons, which caused 3% of the BPI pulses. The BPI pulses were counted in two independent scalers for later use in calculating the cross section.

The spectrometer was designed to accept kaons which were produced in the target at angles between 0° to 4.5°

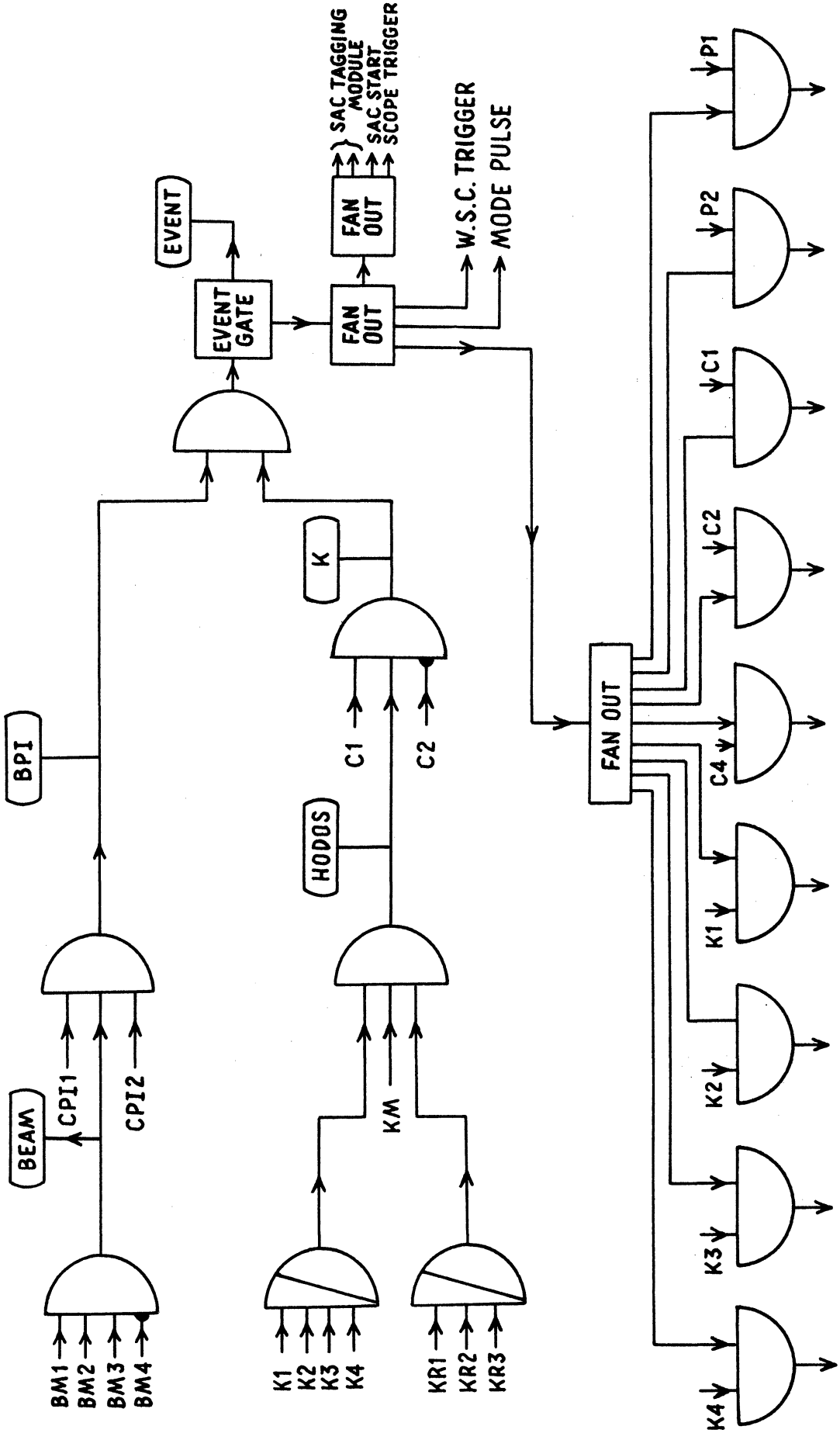

Figure 4. The flow chart of the fast electronics logic.

in the laboratory system. Incident pions which did not interact also went through the spectrometer. The ratio of the K events to the number of incident pions was about 10^{-5}; therefore a pion rejection of the order of 10^{-5} was necessary in order to avoid triggering the apparatus on direct pion beam. A rejection ratio of this order of magnitude was also necessary to kinematically separate the K events, as is explained later. There were three gas threshold focusing Cerenkov counters, C1, C2 and C4, detecting kaons and suppressing the pions in the beam and pions due to elastic and inelastic scattering. The optics and sizes of C1 and C2 were identical. Figure 5 shows the details of C1. The windows of C1 were made of aluminum domes with thickness of .1 in. and .15 in. C1 was designed to detect kaons coming from the target between 0° - 5° by producing Cerenkov light with a cone angle of 4.5°. The solid lines in Figure 5 show the paths of the Cerenkov rays. These rays are reflected on two spherical mirrors and are focused near the photocathode of a 5 in. RCA-4522 photomultiplier, after passing through an iris of 4.5 in. diameter. This iris rejects the Cerenkov rays of a cone angle larger than 4.5°. A ray tracing program was written to check whether all the Cerenkov light in a 4.5° cone produced by the charged particles would go through the iris. It was found that 100% of the rays of 4.5° cone go through the iris and as the cone angle was increased fewer rays went through the iris.

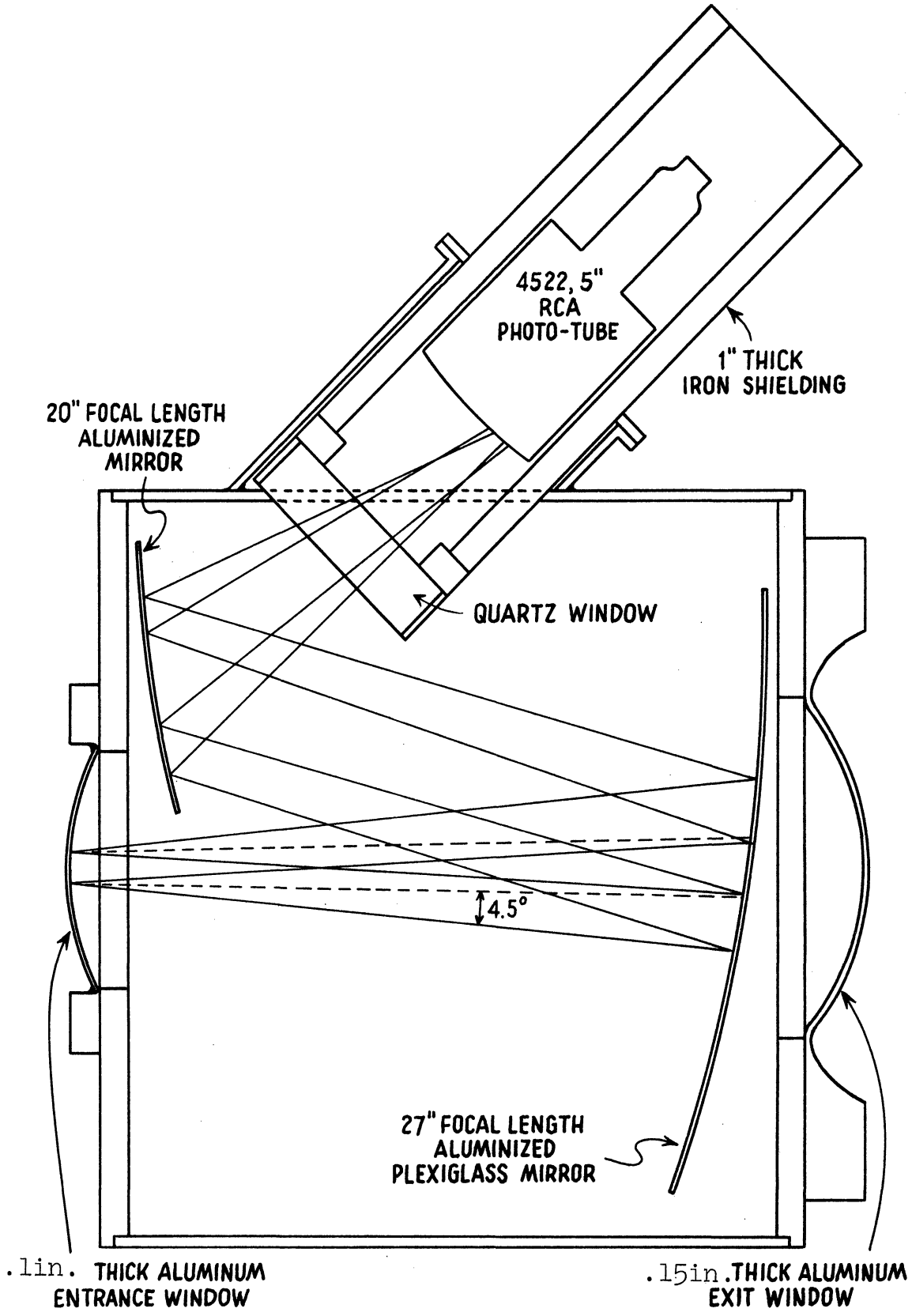

Figure 5. The schematic diagram of the C1 Cerenkov Counter.

Figure 6 shows the pressure curve for C1 for 5 Gev/c incident pions. Freon 13 was used in C1. The solid line is number of events versus pressure while C2 and C4, which were detecting only pions, were taken out of anticoincidence. The solid line shows that pion detection efficiency of C1 started to fall off at 140 psig (pound per squared inch) which corresponded to a cone angle of 7.2° and it was very inefficient at 180 psig (8.5° cone angle) in detecting pions. The dashed line is the number of events versus pressure with C2 and C4 in anticoincidence to reject pions. C1 started counting kaons as well as pions at about 60 psig. It's kaon detection efficiency increased with pressure increase while it's pion detection efficiency remained constant, until the pressure reached about 140 psig. The fall-off of the dashed line at 140 psig is due to the inefficiency of C1 in detecting pions for cone angles larger than 7°. The pressure of C1 was therefore set at 180 psig for detecting 5 Gev/c kaons, where the detection efficiency was independent of pressure for kaons and very small for pions.

C2 was set to detect only pions, and it was in anticoincidence with C1. C4 was a boiler vessel with three spherical mirrors to focus Cerenkov light on the photocathode of three 5 in. RCA-4522 photomultipliers. C4 was used only in tagging bit units and not in the trigger. This was desirable since C4 was not as efficient as C2 and also about 7% of the kaons interacted in the walls of C4. It

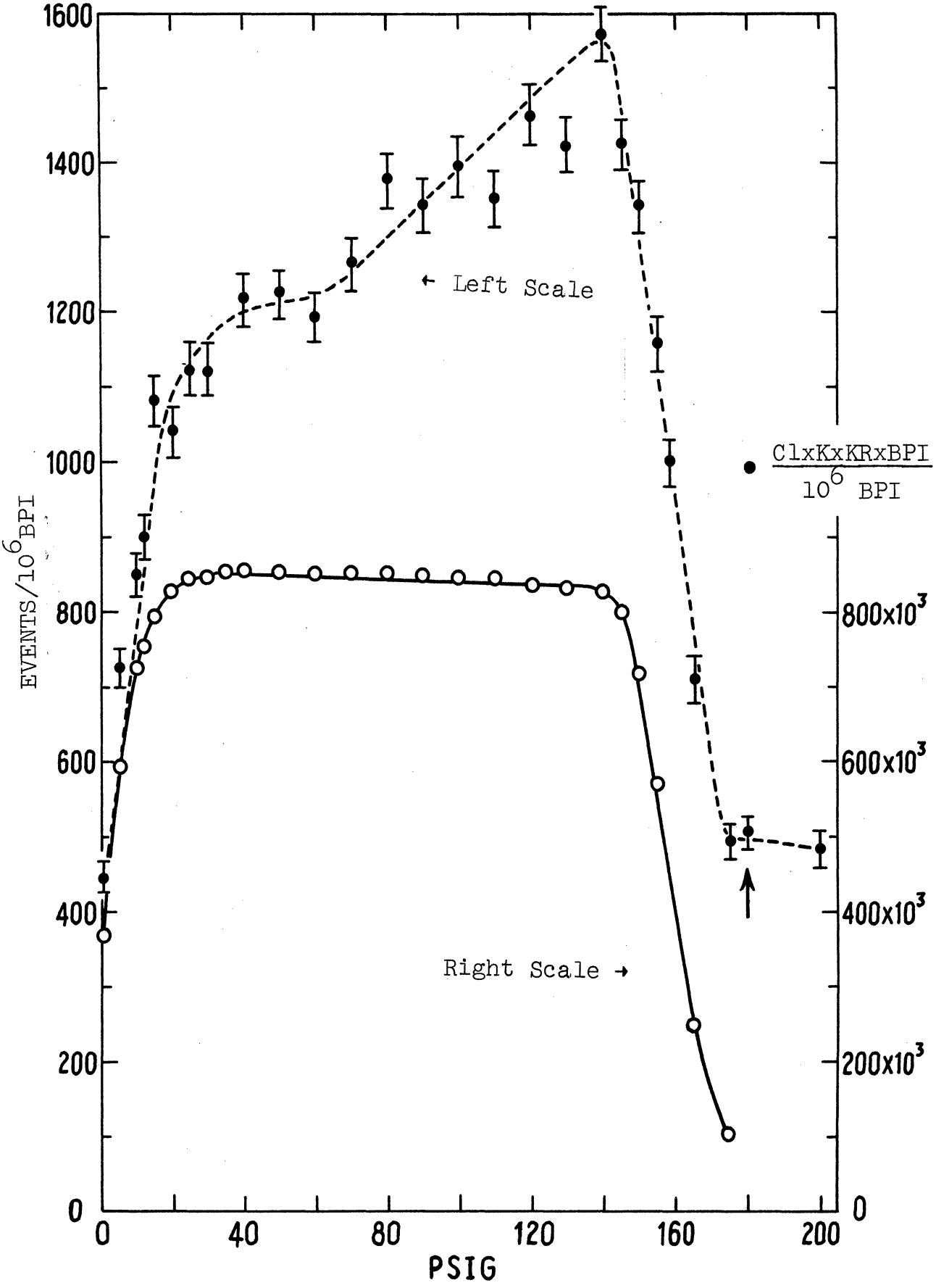

Figure 6. The pressure curve for C1 Cerenkov counter at 5.0 Gev/c incident beam momentum.

will be shown in chapter 3 that the combination of C1, C2 and C4 Cerenkov counters gave a pion rejection of the order of 10^{-6}.

There were three sets of scintillation counters, K1234=(K1, K2, K3, K4) at the entrance of the analyzing magnet, KM at the exit of the analyzing magnet and KR = (KR1, KR2, KR3) behind the last set of the spark chambers K4. This set of scintillation counters was used to detect produced particles and to suppress the triggers on the spurious particles which were coming from different directions. The coincidence, K = HODOS x C1 x $\overline{C2}$, indicated that a kaon passed through the spectrometer. (HODOS = K1234 x KM x KR.) The coincidence between K and BPI formed the EVENT signal, EVENT = BPI x K.

A buffer system (to be explained in detail later) conveyed information from different elements of the experiment to the computer. The EVENT signal triggered the spark chambers and prepared the buffer for a new event. The event signal was set in coincidence with P1, P2, C1, C2, C4, K1, K2, K3 and K4 counters and the computer was told which one of these signals was present when the EVENT was formed. Some of these counters such as P1, P2 and C4 were only in tag bits and not in the trigger. A dead-time of 40 miliseconds was provided by an EVENT GATE module after each event. During this time the ions in the spark chamber were cleared and the buffer system had accepted

all the data and these data were transferred to the computer.

Every ten ZGS pulses, the computer pulse was used to change the trigger requirement (by changing the Cerenkov counter requirement) to select beam pions going through the spectrometer. During the time of this ZGS pulse, scalers were gated off and the wire spark chambers were triggered on the incident beam. These "Mode pulse events" were used to check the magnetic fields of the magnets as well as the apparatus survey. The angular resolution of the spectrometer and the beam momentum and beam momentum resolution were determined from the data accumulated during the mode pulse. This data was also used later to find the wire spark chamber efficiency.

C. The Spark Chambers:

In this section the wire spark chambers are explained in detail and their superiority to optical spark chambers for this experiment is discussed.

A spark chamber consists of two parallel conducting plates, which are connected to a high voltage pulser. The high voltage is turned on after the charged particle has passed through the plates. The charged particle creates positive and negative (electrons) ion pairs and high voltage accelerates these ions. The collision of these ions with the molecules creates many more ions, which causes the spark break-down between the plates. For optical spark chambers, cameras take pictures of this spark for later

analysis.

The wire spark chamber[15-18] is the natural descendant of the usual parallel plate spark chamber. The major difference is the method of extracting the information. In order to make the spark discharge immediately available for processing, the conducting planes are replaced by a layer of parallel wires, typically 0.1 milimeter in diameter and spaced 1. milimeter apart. The discharge current flows through the wire. This current may be detected and used to find which wires have been struck by the spark and thus where the particle has passed through the chamber.

The virtue of using the wire spark chambers in this experiment are; a) they can be triggered on events which have been preselected by a scintillation and Cerenkov counter system; b) they can be connected to an on-line computer, which does a major part of the analysis while the experiment is in progress, where optical spark chambers can not be connected on line to a computer; c) they measure the trajectories accurately.

Five sets of spark chambers were used in this experiment. Each set consisted of four gaps. The sizes of the chambers were from 19 in. x 11 in. to 80 in x 32 in. Figure 7 illustrates the different layers of materials from which a single gap chamber was constructed. There were 30 wires per inch, which were bonded to a mylar film of .002 in. thickness. A 3/8 in. glass epoxyed laminate spacer

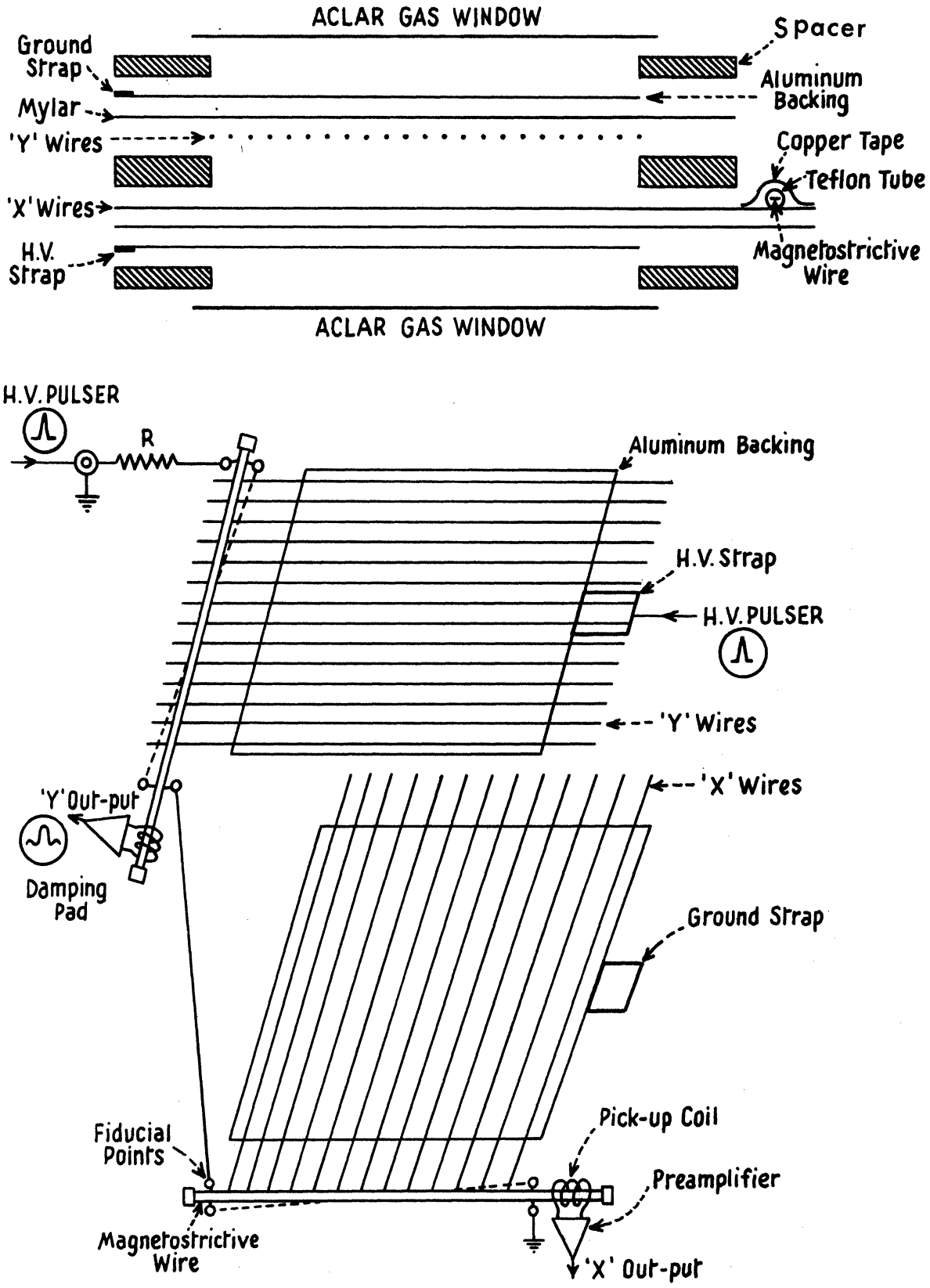

Figure 7. The details of the physical construction of a single gap wire spark chamber.

separated the two planes of mutually perpendicular wires. A continuous sheet of aluminum was bonded to the other side of the mylar sheet. The aluminum sheet and layer of wires, which are separated by the mylar, form a capacitor. The high voltage was applied to the aluminum sheet and by inductance the high voltage was transferred to the wires quickly and uniformly everywhere. A 1/8 in. spacer with an aclar window was epoxyed to the chamber. The gas, which was a 10% helium and 90% neon mixture, filled the space between the two layers of wires and between the aclar window and the aluminum sheet at a pressure slightly higher than atmospheric pressure.

A magnetostrictive ribbon, Remender[19], was magnetized and placed close to and perpendicular to the chamber wires. The discharge current pulse caused a sonic wave in the magnetostrictive ribbon[17]. This wave propagated with the velocity of sound(5 milimeters/microseconds) in the ribbonto to the both ends, where it was damped by clamping the ribbon between rubber pads. At one end of the ribbon a small pick-up coil was located which was connected to a preamplifier. When the sonic wave arrived in the pick-up coil, it induced a voltage in the coil which was of a few tens of milivolts in amplitude. Two fiducial wires were placed across the ribbon, one between the pick-up coil and the wires and one beyond the wires. The fiducials for horizontal and vertical wire planes were connected

in series. The fiducial wire was pulsed at the same time as the wires of the chambers; these fiducial wires also generated sonic pulses. The pulses from fiducials and spark discharges arrived at different times at the pick-up coil. Those time differences were proportional to the differences in distance between fiducial marks and spark-struck chamber wires. The spark positions were determined by measuring the delay time of the sonic pulses caused by the sparkdischarge relative to the same pulses from the fiducials.

A narrow gap chamber requires a current of about 1000 amperes and a potential of several thousand volts and the rise time of the high voltage pulse must be short. A fast rise time is needed to prevent the high voltage pulse from acting as a clearing field, during the rise time, and sweeping away primary ions (caused by the traverse of the charged particle through the gas) before spark discharge develops. Hydrogen thyratron tubes were used to construct a high voltage pulser for these chambers. The schematic diagrams of the high voltage pulser, with a brief discription, are given in Appendix II.

D. The On-line Computer:

One of the great advantages of a wire spark chamber, as mentioned before, is the feasibility of being connected to an on-line computer. The outputs of the individual chamber were transferred to the computer through the buffer

system.

The on-line computer used in this experiment was an EMR (Electro-Mechanical Research, Inc.) 6050. The size of the memory was 16K words, each word being 24 binary bits. Figure 8 shows the different input-output devices such as data buffer, teletype, oscilloscope etc. which were communicating with the computer.

Any input has to be digitized and transferred to the computer sequentially. For this reason a data buffer was used to digitize the analog output of the magnetostrictive read-outs of the spark chambers. A 20 megacycle clock was used to digitize the analog outputs. The buffer accepted the data, digitized and stored the signals from 32 spark chamber read-outs as well as from scintillation and Cerenkov counters and then sent these signals to the computer. The data from the magnetostrictive lines were accepted in parallel by the buffer, but were transmitted serially to the computer.

The buffer system used was the MIDAS (Multiple Input Data Acquisition System) from Science Accessories Corp. There were two SAC units (Enenekontakaihex Scaler Model 1124) which received the signal from 32 magnetostrictive read-outs. One of these SAC units had 96 scalers and the other had 32 scalers. There were four scalers reserved for each magnetostrictive read-out. These four scalers allowed for a maximum of three sparks and one rear fiducial.

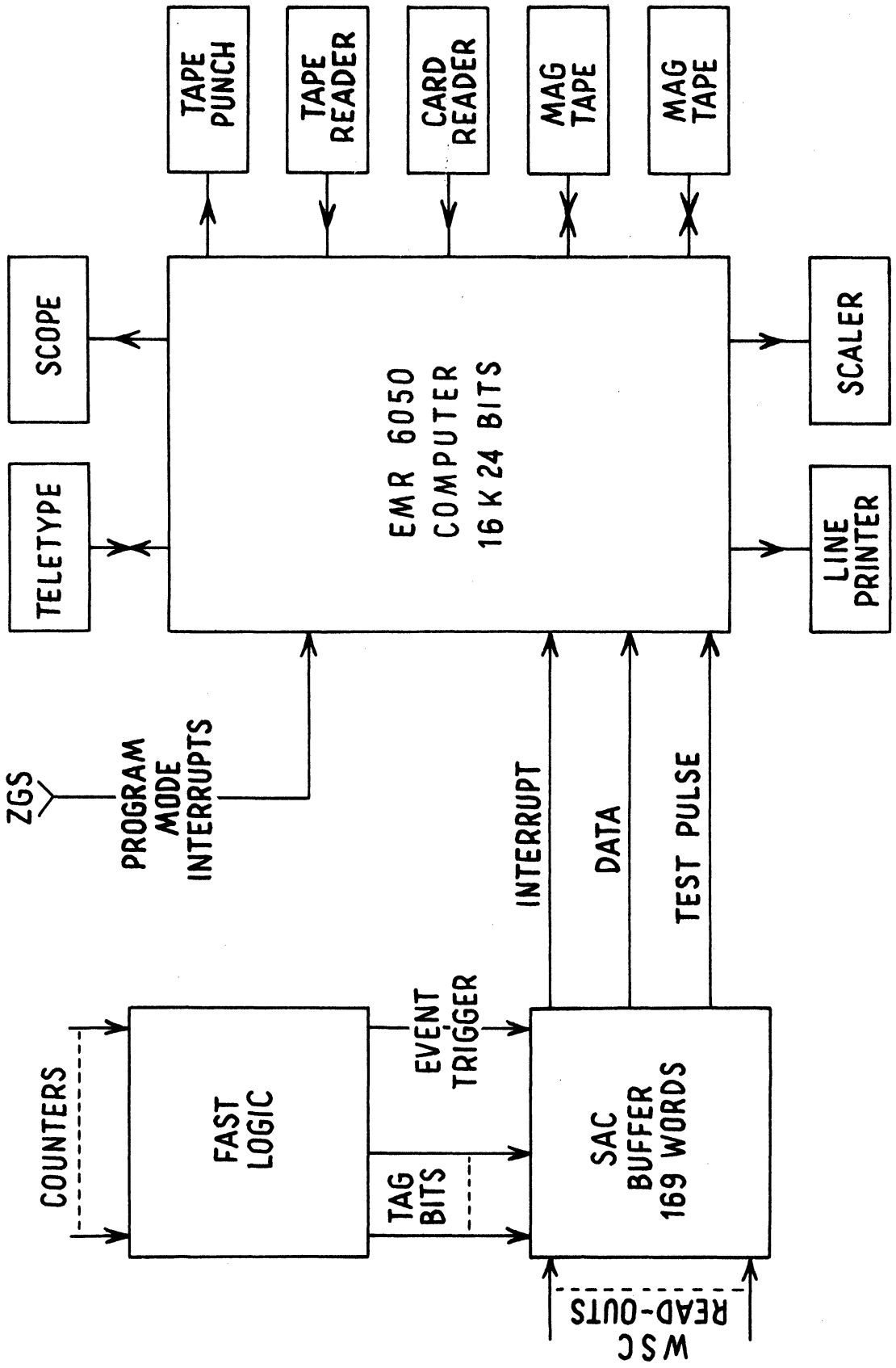

Figure 8. The flow chart of the different input-output devices to the computer.

The EVENT signal, in the fast logic, was set in coincidence with individual counters, K1, K2, K3, K4, C1, C2, C4, P1 and P2. The outputs of these coincidences were sent to the SAC buffer (model 1105 Gated Tagging) and then to the computer. In this way when the EVENT was formed, it could be found which of the above counters had pulsed.

A Multiplexer (SAC Model 1118) was connected to the Differential Voltmeter (DVM) output for magnet current and also to the Analog to Digital Converter (ADC) for transferring pulse height information on C1 and C2 Cerenkov counters to the computer.

When the EVENT GATE module, in the fast logic, received the event signal, it turned off the fast logic gates for 40 milliseconds and no data was accepted during this period of time. The EVENT GATE sent a signal to the buffer and a signal to the high voltage pulser to pulse the spark chambers. The arrival of an EVENT signal from fast logic to the buffer caused the scalers to reset to zero and to clamp there for 15 microseconds. The reason for this dead time is that when the chambers are pulsed, there will be an electromagnetic noise broadcast, which can be picked up by the pick-up coil and be mistaken as a fiducial or spark pulse. When this clamp was lifted, the scalers stayed at zero until the first pulse from the chamber reached the buffer. The first pulse, which was assumed to be from the

first fiducial, started all four scalers reserved for that magnetostrictive line. The computer program checked the last spark to see if it was close to the expected rear fiducial position; if it was not, the computer used the rear fiducial position from the previous set of sparks. The successive sparks locked the successive scalers. These scalers generated a binary number corresponding to the position of the spark. The content of these scalers were read by the master control unit of the buffer (SAC Model 1204) and transmitted to the computer.

When the computer had received all the data during the spill time, it first sent these data to the magnetic tape for future off-line analysis and then started the calculation. Along with the calculation, it sent the results to the display oscilloscope. The display oscilloscope was very essential for diagnostic purposes. It displayed various histograms, such as missing mass, four momentum transfer distribution of the cross section, etc. It also displayed a computer simulation of the tracks through the chamber. These histograms and the computer simulation were helpfull for understanding how the different parts of the equipment were functioning and what results the experiment was producing.

A test pulse was provided for testing the buffer and the on-line computer communication. The computer, after receiving a signal from the ZGS, sent a pulse to the buffer

through a Test Generator (Model 1110). The Test Generator sent a sequence of signals, resembling the signals from the chambers, to the buffer. These signals were sent to the computer by the buffer in the same way that event data were produced. Later, the computer checked this test pulse to find out whether the buffer had responded properly to the test pulse. This was a check of the communication line between the buffer and the computer. The buffer and the computer started accepting data after the test pulse, during the 500 milliseconds of the ZGS spill time. The test event took about one millisecond.

III. DATA ANALYSIS

A number of steps are required to derive final differential cross sections from the spark coordinates stored in the computer. The major steps will be outlined here and then discussed in detail in the various subsections of this chapter.

The first step in the analysis consists of assembling the sparks in each chamber into tracks if possible, and if not possible, in rejecting that set of sparks as an event candidate. This procedure and corrections introduced by it are discussed in section A. The tracks from the first step are then connected up to form possible orbits for the spectrometer particle and the beam particle. At this point,a number of geometric and kinematic criteria (cuts) are imposed on good events. We discuss the cuts and corrections required by them in section B. Section B also describes the calculation of kinemetic quantities such as kaon production angle and momentum from the orbit information.

The analysis described so far is done event by event on line by the computer. At the end of each run the computer printed out histograms in missing mass, four momentum transfer and in other variables of interest. The final step in the analysis consisted in applying corrections for geometrical acceptance and various nuclear

absorption and decay effects to the raw computer histogram. These corrections and the calculations of the differential cross section are described in sections C through F.

A. Track Reconstruction and Spark Chamber Efficiency:

There were four sets of spark chambers (each set consisted of four gaps) in the spectrometer and one set in the incident beam-line. These chambers did not always form detectable sparks for the desired charged particles which went through the system. There were some occasions when there were spurious spark tracks. These spurious sparks took the discharge energy of a good track, sometimes they reduced the amplitude of the magnetostrictive readout to below the threshold of the buffer and therefore that good track was either completely lost or there were two adjacent tracks, which confused the filter program.

To define the trajectory, there was required the presence of tracks in each of the four horizontal views (K1, K2, K3,K4), two vertical views (K1 and K4) and tracks in the horizontal and vertical views of the beam chambers. A good unique track has only three or four detectable sparks in a set, that can be fit to a straight line within a given accuracy. If a set had a good track (3 or 4 sparks), the program fitted a straight line to these sparks and compared the measured position of each spark relative to the expected position. The distance

between measured and expected position must be within a given accuracy.

The horizontal view efficiency of one set was found by finding the probability that the corresponding set had a good unique track while at least two other sets also had a good unique track (this included two spark tracks too). The horizontal view efficiency varied from 96% to 99% for all the chambers and it was fairly constant over the range of -t acceptance. The Mode pulse, which was explained previously, was used to find the spark chamber efficiency;since most of the mode pulse events contained single non-interacting tracks going straight through the chamber, the determination of this efficiency was relatively easy.

The two chambers K1 and K4 determined the vertical position of the trajectory as well as the horizontal position. The vertical view efficiency of each set was determined by finding the number of times that it had a good unique track while all the horizontal views had a good track. The vertical view efficiency was from 97% to 99%. Beam chamber efficiency was found by asking the number of times that each view, horizontal or vertical, had a good track while the spectrometer chambers had a good trajectory. The beam chamber efficiency was from 94% to 97%. The overall efficiency of five sets of chambers were the products of the efficiency of each set. The final chamber efficiency correction applied to the cross section was 80% for 5 Gev/c and 85% for 3 and 7 Gev/c incident beam momentum.

B. Event Reconstruction and Cut Requirements:

The major background in this experiment was from particles produced in the C1 Cerenkov counter or upstream of the hydrogen target. In order to reduce this background, it was required that the kaon had originated in the liquid hydrogen target.

The computer program chose a center value for every good track in every set of chambers. The center values of K1 and K2 sets formed a line indicating the particle trajectory entering the momentum analyzing magnet (BM-109) and the center values of K3 and K4 formed a line indicating the particle leaving the bending magnet. These two lines are expected for kinematic reasons to intersect at the center of the magnet. A good event was required to have tracks intersecting within $\pm.5$ in. Figure 9 shows the distribution of the separation between the incoming and outgoing trajectories through the magnet at the center of the bending magnet. The magnet cut rejection was negligible.

The momentum of the spectrometer particle was found from;

$$P = \frac{\int \vec{B}.d\vec{l}}{1313.2(\sin\theta_i + \sin\theta_f)} \qquad (10)$$

where θ_i and θ_f are the plan view angles that incoming and outgoing particle trajectories make with the longitudinal axis of the bending magnet. $\int \vec{B}.d\vec{l}$ is the magnetic field integral of the magnet. The momentum resolution of the spectrometer, which is due to measurement error in θ_i and θ_f, was found to be $\pm 3/4\%$. The momentum resolution of the incident pion beam was found to be .63%. Therefore, the total momentum resolution of the system was .98%.

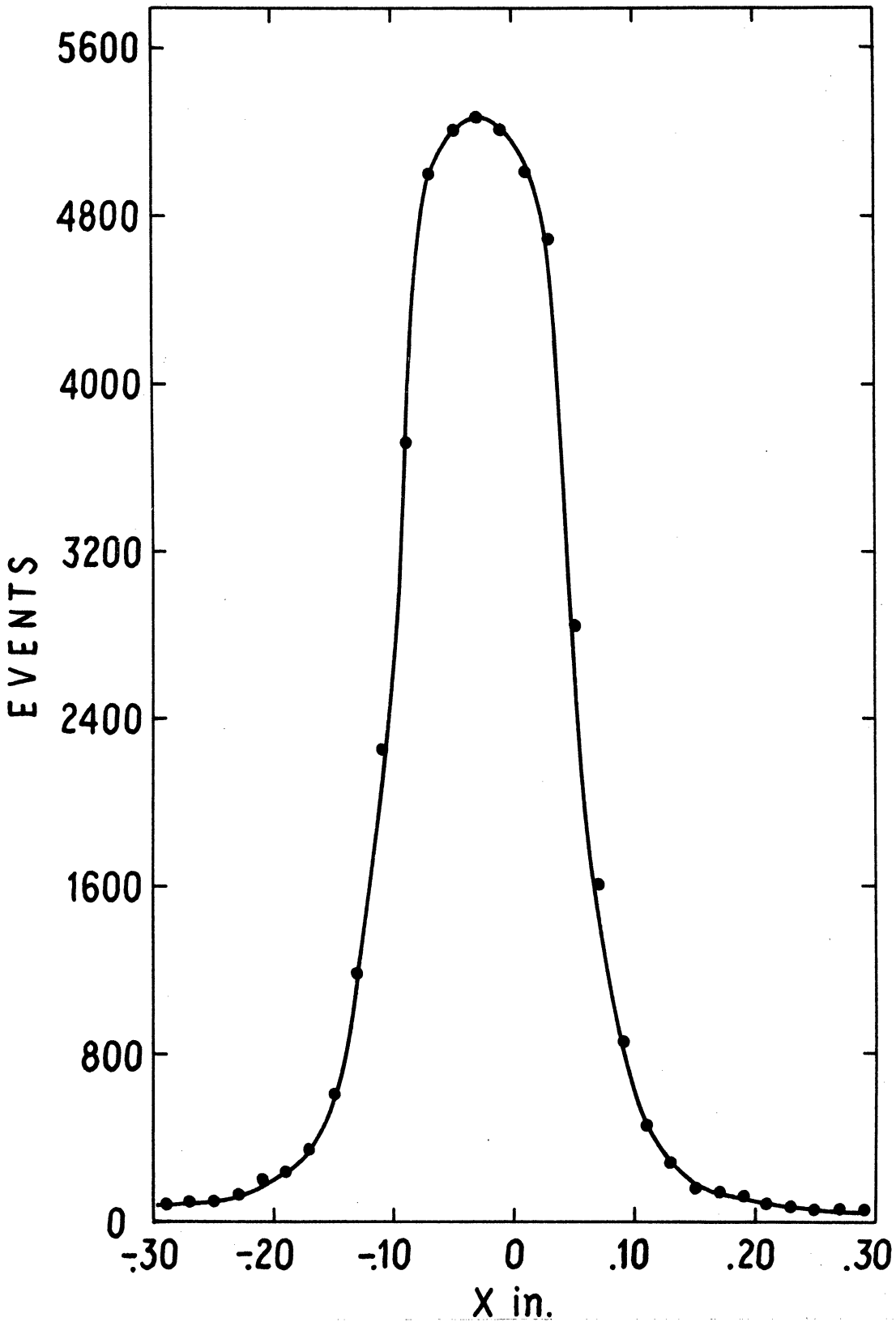

Figure 9. The distribution of the separation between the incoming and outgoing trajectories through the magnet.

The missing mass of every event was calculated from equation 9 after the event was momentum analyzed. The mass resolution of the spectrometer was found to be 40 Mev. The missing mass of $K\Sigma$ candidates were required to be within the mass limit; $Mass_{\Sigma}^{2}$ ($1 \pm .195$). This mass limit was three times of the RMS of the mass resolution of the spectrometer for the Σ peak. There were practically no events outside the mass cuts for Σ events after target out subtraction. Figure 10 shows the missing mass plot after target out subtraction at 5 Gev/c.

The particle trajectory was traced back to the hydrogen target and the production point of the particle was calculated. In order to reduce background from out of target production, the X and Y coordinates of the production point were required to be within $\pm$ 1.2 in. and the Z-coordinate within the $\pm$ 24 in. of the center of the target. Multiple coulomb scattering in C1 and C2 Cerenkov counters caused a displacement of the production point, in tracing back the trajectory to the hydrogen target, by .12 in. (one standard of deviation). The cuts of $\pm$ 1.2 in. in both X and Y directions were ten times larger than the coulomb scattering effect. Therefore there were practically no true events outside of the cuts. Figure 11 shows the X distribution of the events before and after Y cut requirement. The effect of the Y cut in eliminating out of target background is clear.

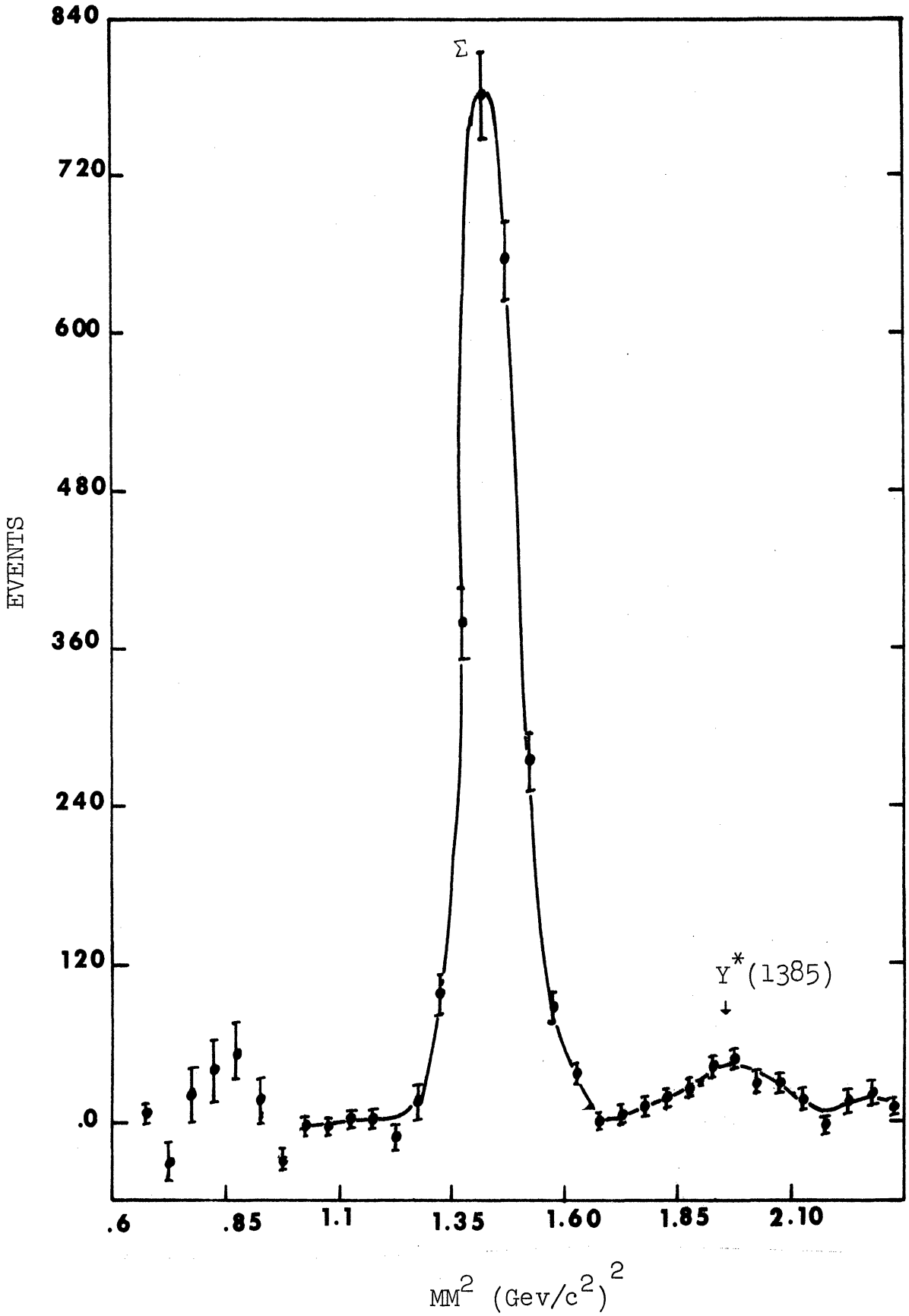

Figure 10. The missing mass plot for the Σ and the Y^* production after target out subtraction.

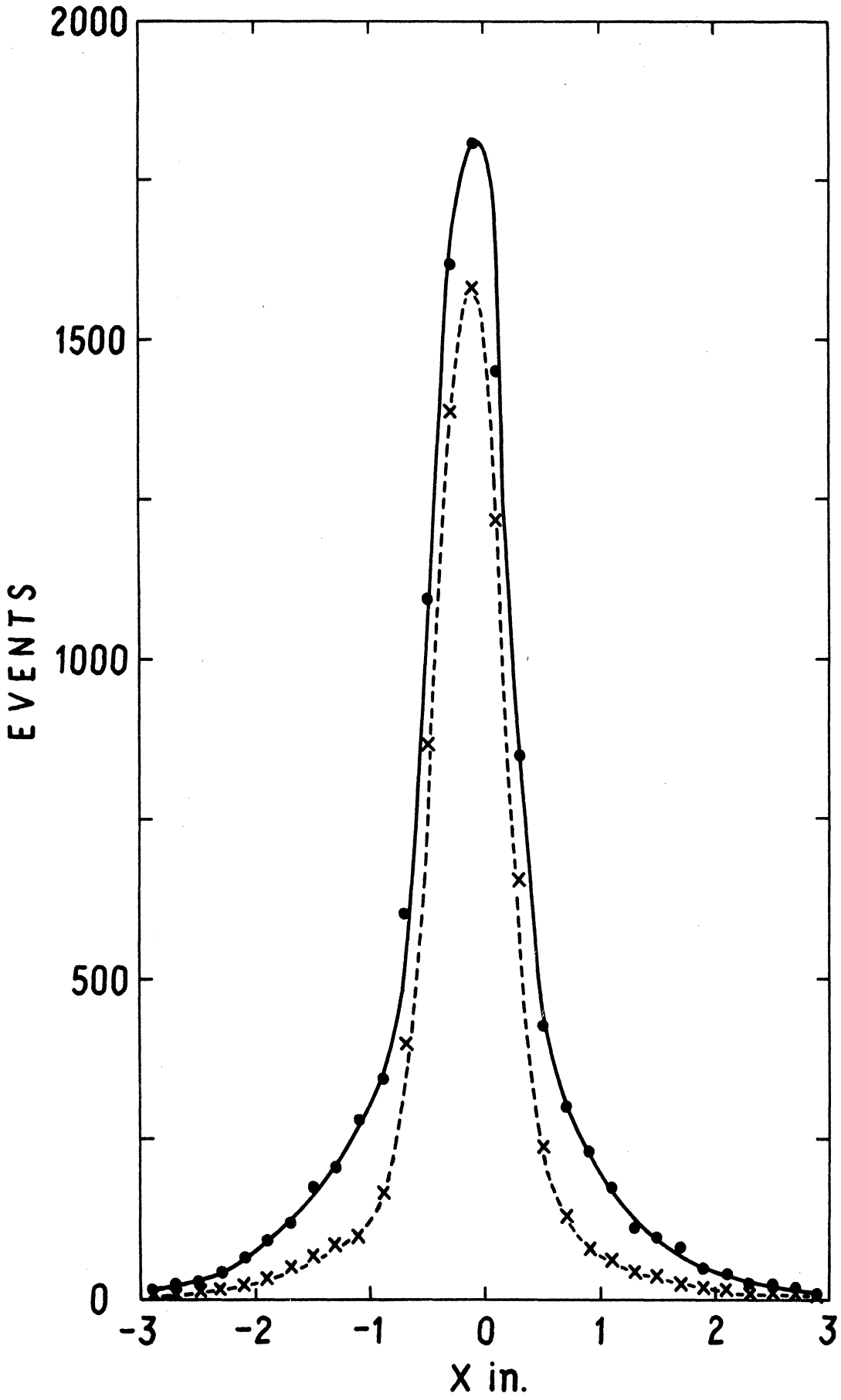

Figure 11. The X distribution of the events before and after Y cut requirement.

The target cut requirement eliminated most of the background due to Cl and sources upstream of the H_2 target. The target empty runs indicated that about 40% of the events in the zero degree production bin were not produced in the hydrogen target. The target cut requirement could not eliminate these zero degree background events because the Z coordinate of the event origin could not be determined for these events. There were from 0. to 10% target out events at larger angles. The residual background mentioned above was eliminated by subtracting the events from target empty runs. Figure 12 shows the missing mass spectrum without target out subtraction and Figure 10 shows the same missing mass spectrum after the target out subtraction.

The computer printed out several histograms of events at the end of each run. One of these was the squared four momentum transfer distribution of the desired reaction after fulfilling all the cut requirements. This histogram was used to calculate the cross section for the Σ production. In order to subtract the background, in the case of Y^* production, it was convenient to use the missing mass histograms for a variety of angular ranges. Y^* events were divided into five angular ranges 0.-1.4, 1.4-2.1, 2.1-2.8, 2.8-3.5 and 3.5-4.2 degrees. Figure 13 shows the missing mass plots in the above angular ranges. It is clear that the Y^* peak sits on a large background at smaller angles. The Y^* peak increases and the background decreases at larger angles. To find the number of

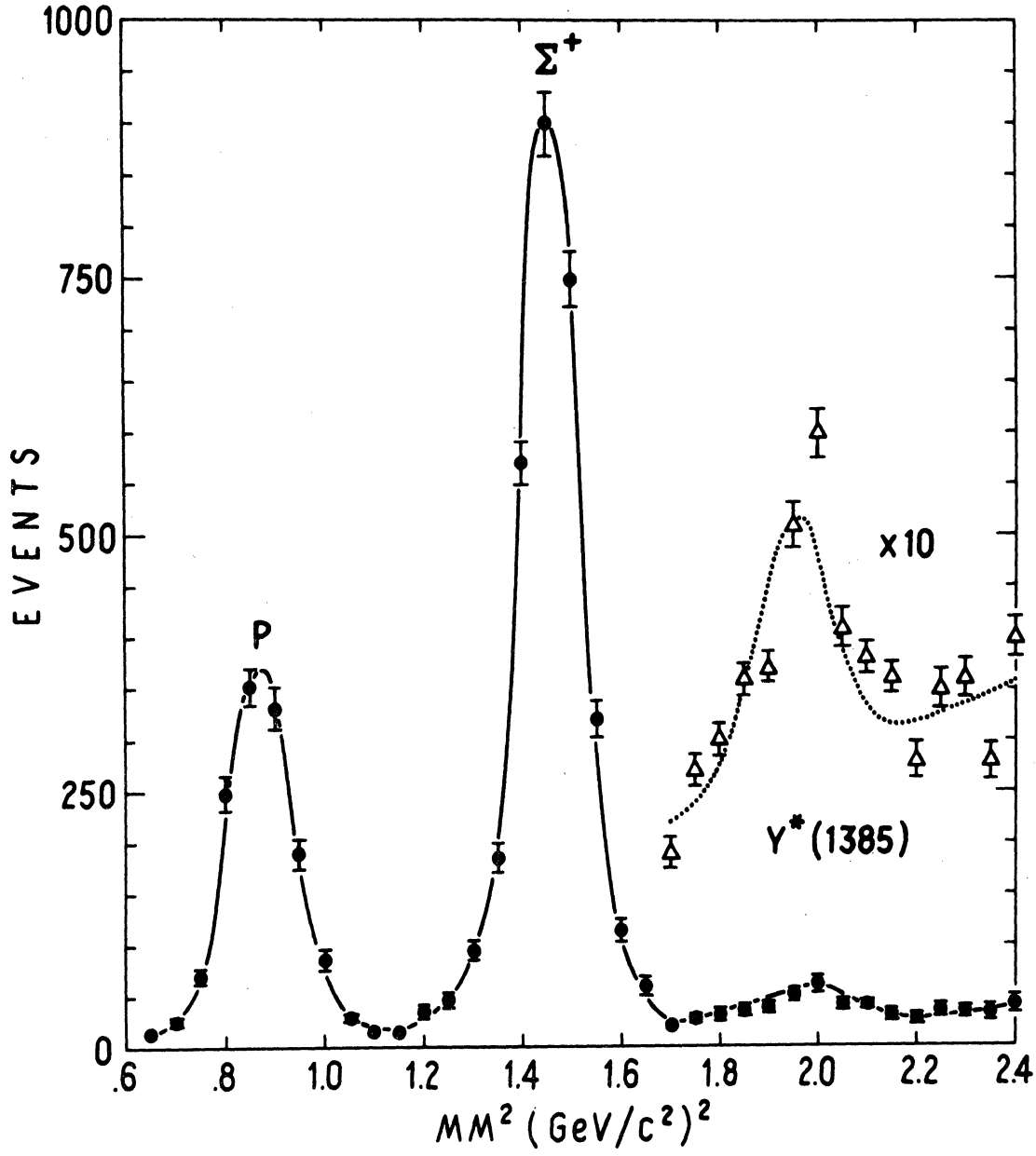

Figure 12. The missing mass plot for the Σ and the Y^* production.

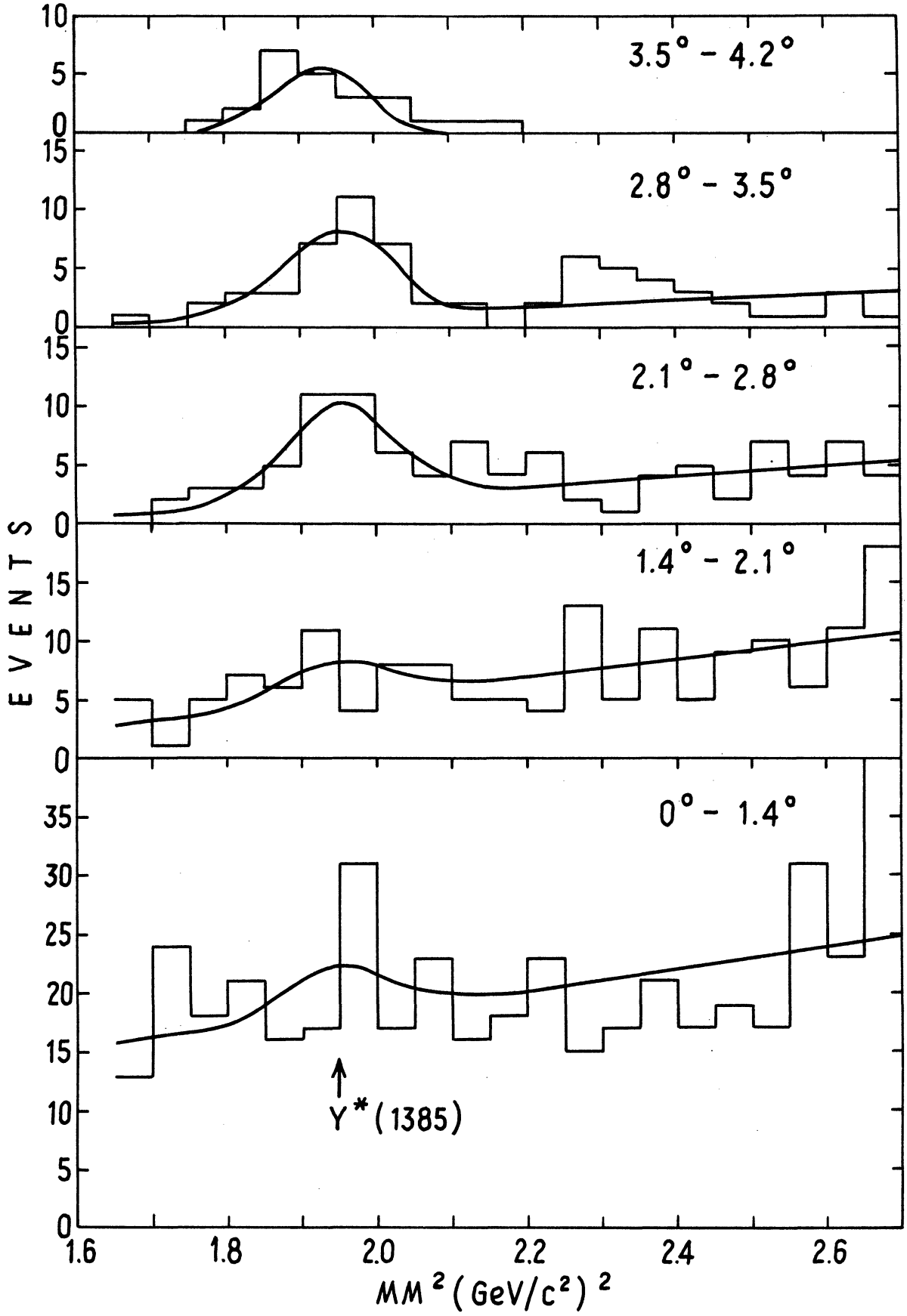

Figure 13. The missing mass spectrum for the Y^* production.

events in the above angular ranges, a mass distribution consisting of a Gaussian with a fixed width and center and a superimposed straight line was fitted to the events in each angular range. The width of the Y^* Gaussian was calculated from the Y^* resonance width folded by the mass resolution of the spectrometer. The smooth curves in Figure 13 represent the fit and the histograms represent the data.

C. Solid Angle Acceptance of the Spectrometer:

Figure 14 shows an end view of the down stream end of the analyzing magnet as was seen by a particle leaving the H_2 target. Consider particles that left the target with polar angles between θ and $\theta + d\theta$. These particles could have any azimuthal angle, but only those particles which passed through the solid shaded section of the annular region between θ and $\theta + d\theta$ would have been accepted by the spectrometer (Figure 14). Therefore, only the fraction $\alpha/2\pi$ of particles with production angle θ was accepted. The spark tracks of the good events had to be within the fiducial line boundaries which was set on the last spark chamber. These fiducial boundaries were determined from the dimensions of the analyzing magnet aperture. The squared four momentum transfer, $-t$, is related only to the polar angle θ and not azimuthal angle φ. By knowing the number of particles accepted between θ and $\theta + d\theta$, it is easy to calculate the number of particles which are accepted with

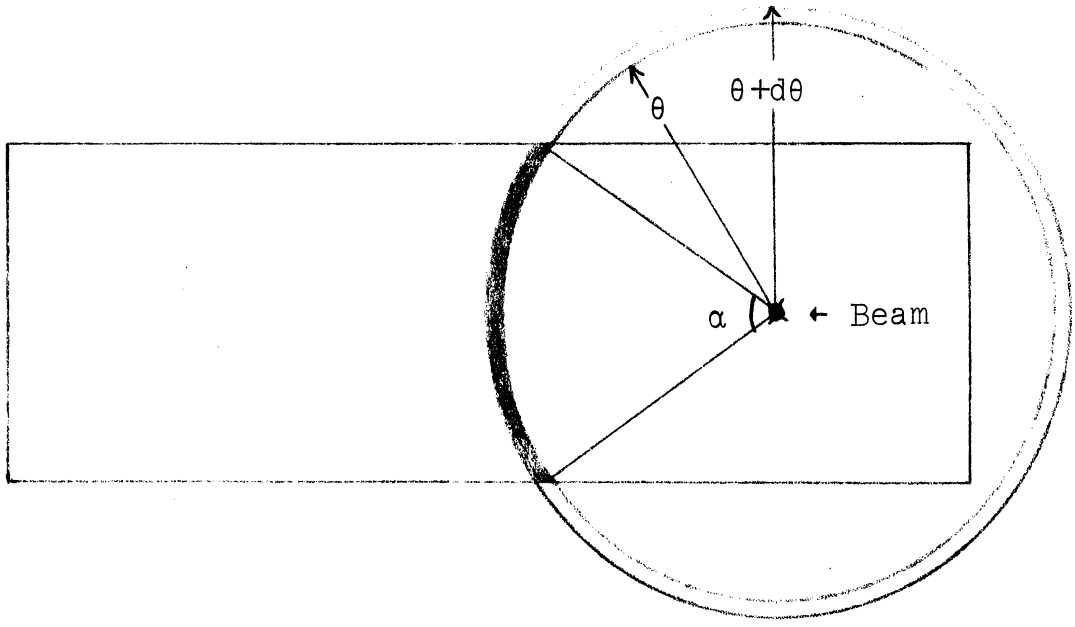

Figure 14. An end view of the down stream end of the analyzing magnet as was seen by a particle leaving the H_2 target.

-t between -t and -t + d(-t).

A Monte Carlo calculation was performed to find the angular acceptance of the spectrometer. Some additional factors, aside from the fiducial boundaries, which were considered in this program were the angular, position and momentum distribution of the incident beam and also the multiple coulomb scattering. The angular and position distribution of the incident beam were found by using the information from the beam chamber. The horizontal and vertical angular distribution of beam particles were consistant with Gaussians having RMS angles of 3.4 and 5.3 miliradians. The position distributions were also consistent with Gaussians having RMS distances of .28 and .22 in. in X and Y planes. The distribution of the beam density was considered to be uniform along the 24 in. hydrogen target for the purposes of the acceptance calculation. The momentum distribution of the beam was consistant with Gaussians having RMS of .63%. The multiple coulomb scattering in the hydrogen target and the two Cerenkov counters C1 and C2 were also considered in determining this angular acceptance. Figure 15 shows the acceptance of the spectrometer as a function of the squared of the four momentum transfer for 5 Gev/c incident momenta.

D. The Incident Beam Correction:

The incident pion beam had a contamination of muons

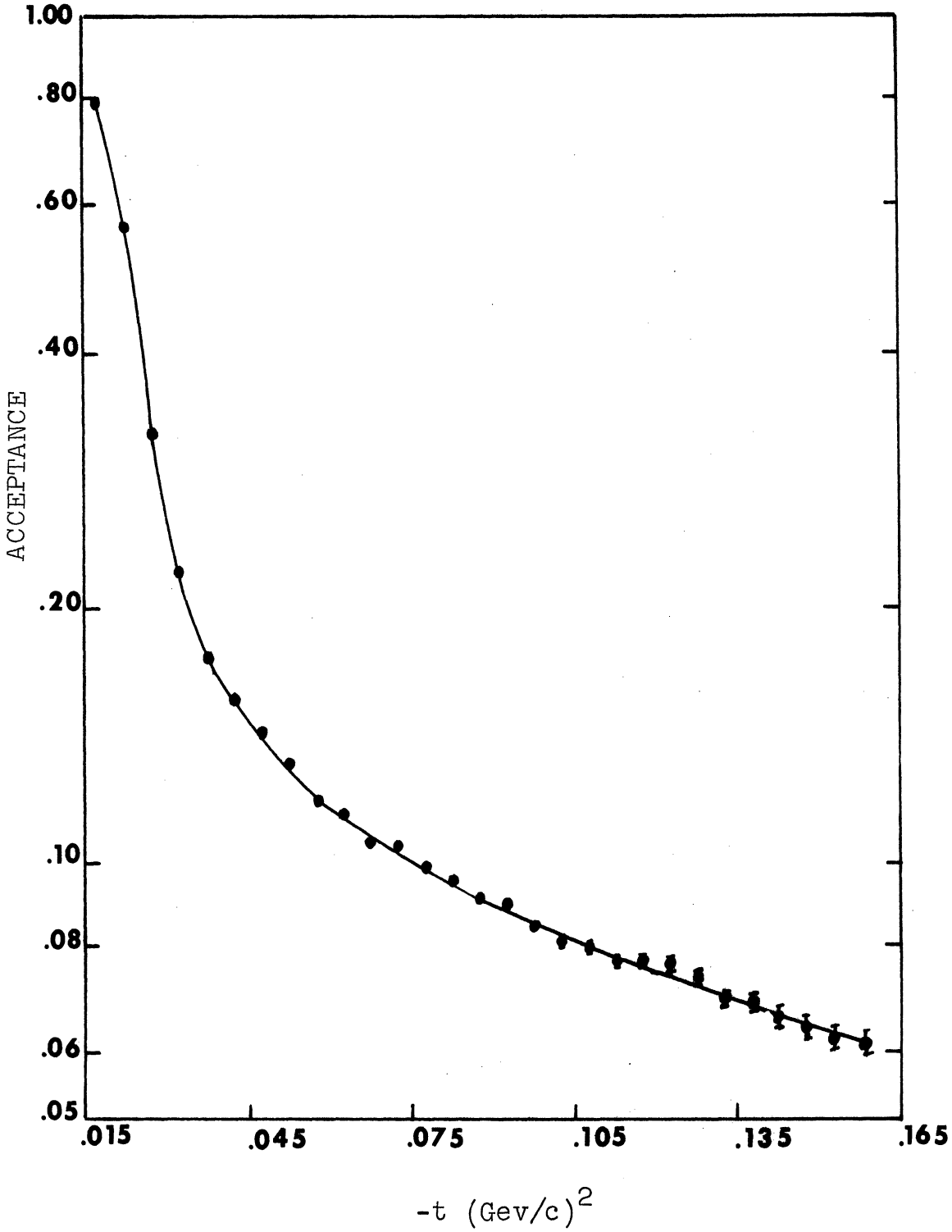

Figure 15. The four momentum transfer acceptance for 5. Gev/c.

and positrons. This contamination was taken to be 3%.[20] The last pion Cerenkov counter in the beam, CPI2, was at a distance of 80 in. from center of the target. A correction was made for the decay of pions in this distance. In the case of the target empty data, the distance from CPI2 to the center of C1 Cerenkov counter was considered for the decay of pion beam since the effective target was C1. Table 2 shows the summary of all the major corrections which was applied to the data. For calculating the absorbtion of pions and kaons in the target, it was assumed that on the average a pion travels half the length (12 in.) of the hydrogen target and produces the kaons and the kaons travel the second half. The same assumption was made in the case of the target out data except that C1 was considered as the target.

E. Nuclear Interaction and Decay Corrections of Kaons:

The produced kaons interacted in the hydrogen target, Cerenkov counters, scintillation counters, air and wire spark chambers. The major interactions were in the C1 Cerenkov counter and the target. The number of good beam pions and kaons eliminated by a material can be readily calculated once the nuclear cross section for that material is known. The wood-Saxon potential was used to calculate the total cross section for various nuclei (Appendix III). The results of this model were in good agreement with experimental data on the total cross sections of pions on various nuclei.

Table II

The summary of the corrections applied to the data

Nature of the correction	3. Gev/c	5. Gev/c	7. Gev/c
Muon and positron contamination	3%	3%	3%
Decay of pions between CPI2 and H^2 target (C1)	1.2%(2.3%)	.73%(1.3%)	.52%(.98%)
Absorption of pion(kaon) in 12in. Of H^2 target	3.51%(2.21%)	3.51%(2.21%)	3.51%(2.21)
Absorption of pion(kaon) in half length of C1	5.85%(3.83%)	4.05%(2.71%)	2.75%(1.95%)
Absorption of kaon in the materials of the spectrometer	13.91%	11.49%	9.77%
Decay of kaon	34.81%	21.57%	15.63%
Spark chamber efficiency	80%	85%	85%
Nuclear interaction in C4	6.90%	6.68%	5.67%
Target out subtraction near 0. degree, at larger angles	40% 0.-10%	40% 0.-10%	40% 0.-10%

A correction was also necessary for those events for which the kaon was misidentified by C4. The C4 Cerenkov counter was only in tag bits, counting only pions, as explained previously. The walls of C4 were made of 3/8 in. steel. The kaons produced at the hydrogen target, which satisfied the trigger condition, can interact in the walls of C4 and produce particles which might be counted in C4. Because C4 was set to detect pions, the computer program rejected the events for which the C4 tag bit was present, but it saved these events in a missing mass histogram. By using the number of Σ events in this missing mass histogram and the number of Σ events in the missing mass plot 12, it was found that about 7% of the time the kaon interacted in the walls of C4 and was counted as a pion.

There was a distance of about 330 in. from the center of the target to the last hodoscopes KR for the kaon to travel and fire the trigger system. A correction for the decay of the kaons in this distance was applied to the data.

The corrections for the absorption and decay were applied separately to the target full and target empty events. It was assumed that most of the target empty events result from interaction of beam particles in the C1 Cerenkov Counter. Therefore the geometry of these counters was used in calculating the corrections.

F. The Differential Cross-Section:

The differential cross section was calculated from;

$$\frac{d\sigma}{dt} = \frac{ne}{nb \times nt \times dt}(\text{ corrections }) \qquad (11)$$

where ne is the number of events in an interval dt, nb is the number of beam pion entering the hydrogen target and nt is the number of protons per centimeter squared in 24 in. long target. The cross sections for the reactions $\pi p \rightarrow K\Sigma$ and $\pi p \rightarrow KY^{*}(1385)$ are summarized in the table III. Figure 16 shows the -t distribution of the cross section for the reaction $\pi p \rightarrow K\Sigma$ and figure 17 shows the -t distribution of the cross section for the reaction $\pi p \rightarrow KY^{*}$ from this experiment together with results from a previous experiment at larger angles.[10,13] The error bars are statistical only. The possible systematic errors are less than 10%.

$\pi^+ + p \rightarrow K^+ + \Sigma^+$						$\pi^+ + p \rightarrow K^+ + Y^*(1385)$	
3.0 Gev/c		5.0 Gev/c		7.0 Gev/c		5.0 Gev/c	
-t	dσ/dt	-t	dσ/dt	-t	dσ/dt	-t	dσ/dt
.0291	685±34	.0246	405±17	.030	229±12	.0365	7.9±5.5
.0331	672±40	.0446	312±18	.070	153±11	.0515	10.7±6.4
.0381	619±33	.0646	305±20	.110	112±10	.0720	28.8±6.6
.0441	543±38	.0846	220±20	.150	67±8	.0990	27.0±6.5
.0511	486±32	.1046	183±18			.1320	24.7±5.7
		.1246	170±18				
A=713.4±23.5		A=411.7±12.2		A=274.9±8.6			
b=14.68±.92		b=9.37±0.16		b=9.01±.21			

Table III. $d\sigma/dt$ in μ b(Gev/c)$^{-2}$ for reactions (5) and (6) and best fits to the $d\sigma/dt = A * \exp[b*(t-t_{min})]$

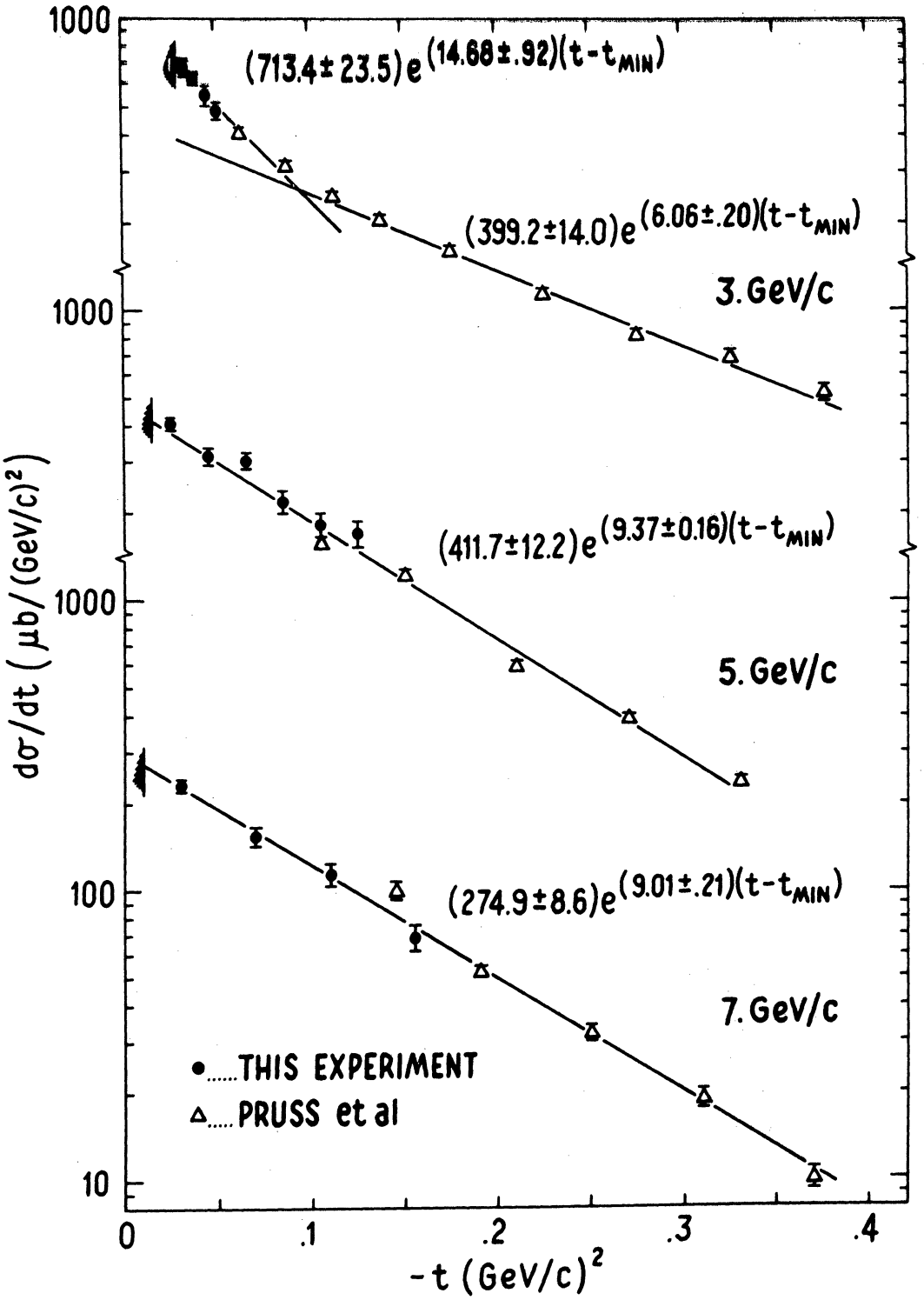

Figure 16. The differential cross sectuon for the reaction $\pi^+ + p \rightarrow K^+ + \Sigma^+$.

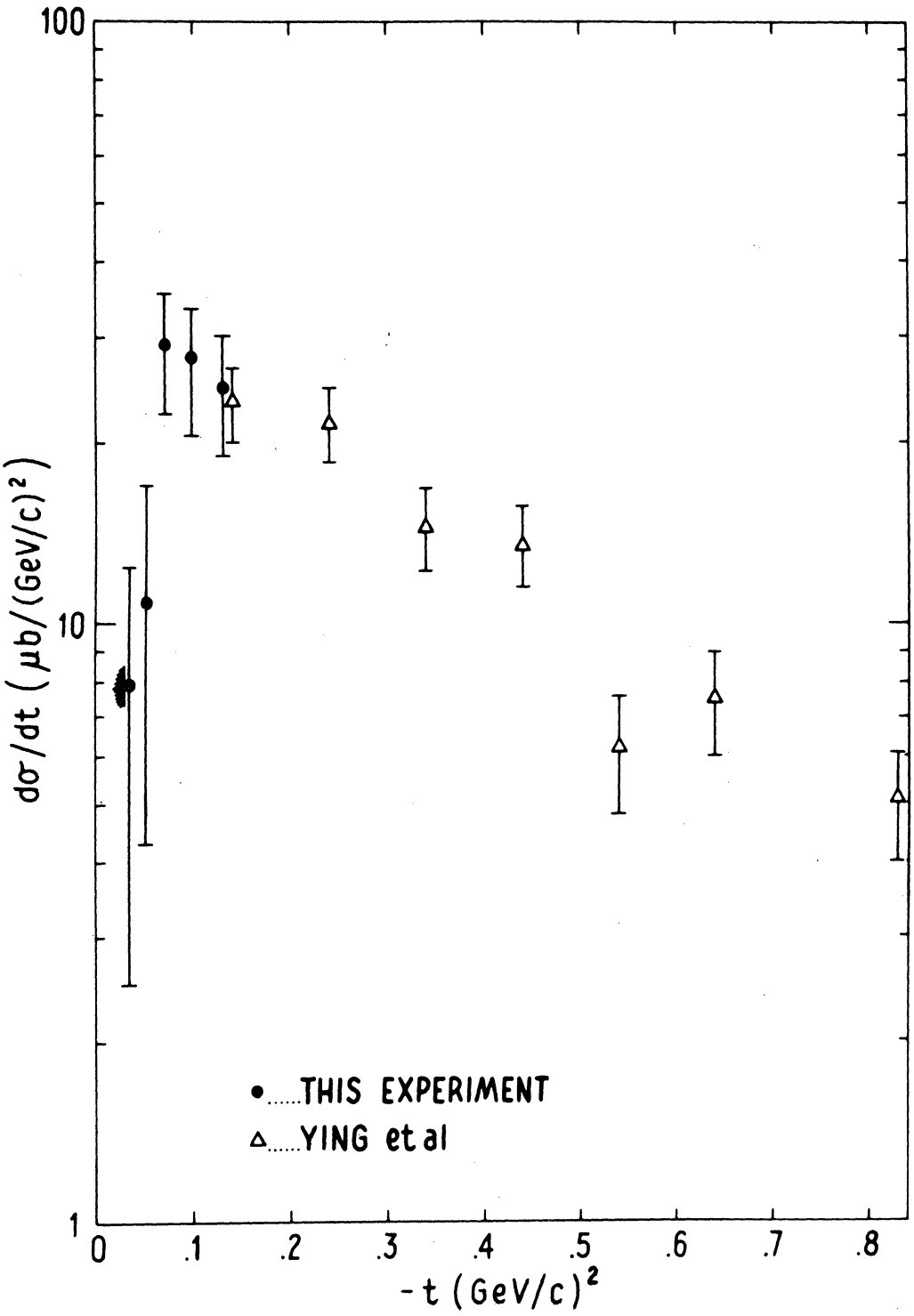

Figure 17. The differential cross section for the reaction $\pi^+ + p \rightarrow K^+ + Y^{*+}(1385)$.

IV. DISCUSSION OF THE RESULTS

The discussion will be divided into four major parts. A) We compare our results with the other cross section measurements on the reactions $\pi^+ + p \rightarrow K^+ + \Sigma^+$ and $\pi^+ + p \rightarrow K^+ + Y^*$ for the purpose of testing the relative normalization of the different measurements. B) We survey the general features of our data on $K\Sigma$ production and compare the data with the Regge pole model. C) We compare our results on the reaction $\pi^+ + p \rightarrow K^+ + Y^*$ with other measurements on this reaction and survey the general features of this reaction. D) We discuss quantitatively the helicity flip and helicity non-flip amplitudes for the above reactions in the final section.

A. Consistency of This Experiment With Other Experiments:

Figures 16 and 17 show the consistency of this experiment with a previous experiment[10,13] on the same reactions which was done at larger angles. The agreement between these experiments at 5 and 7 Gev/c, in the region for which the data overlaps, is excellent. The data of this experiment and the larger angle data[10] were therefore used together to find the slope and amplitude of the cross section as a function of -t. The two sets of data were also used together for comparison with theoretical models and for comparison with measurements of this reaction by other groups. The Stony Brook group[12] has measured the differential cross section for the reactions (5) and (6) for energies from

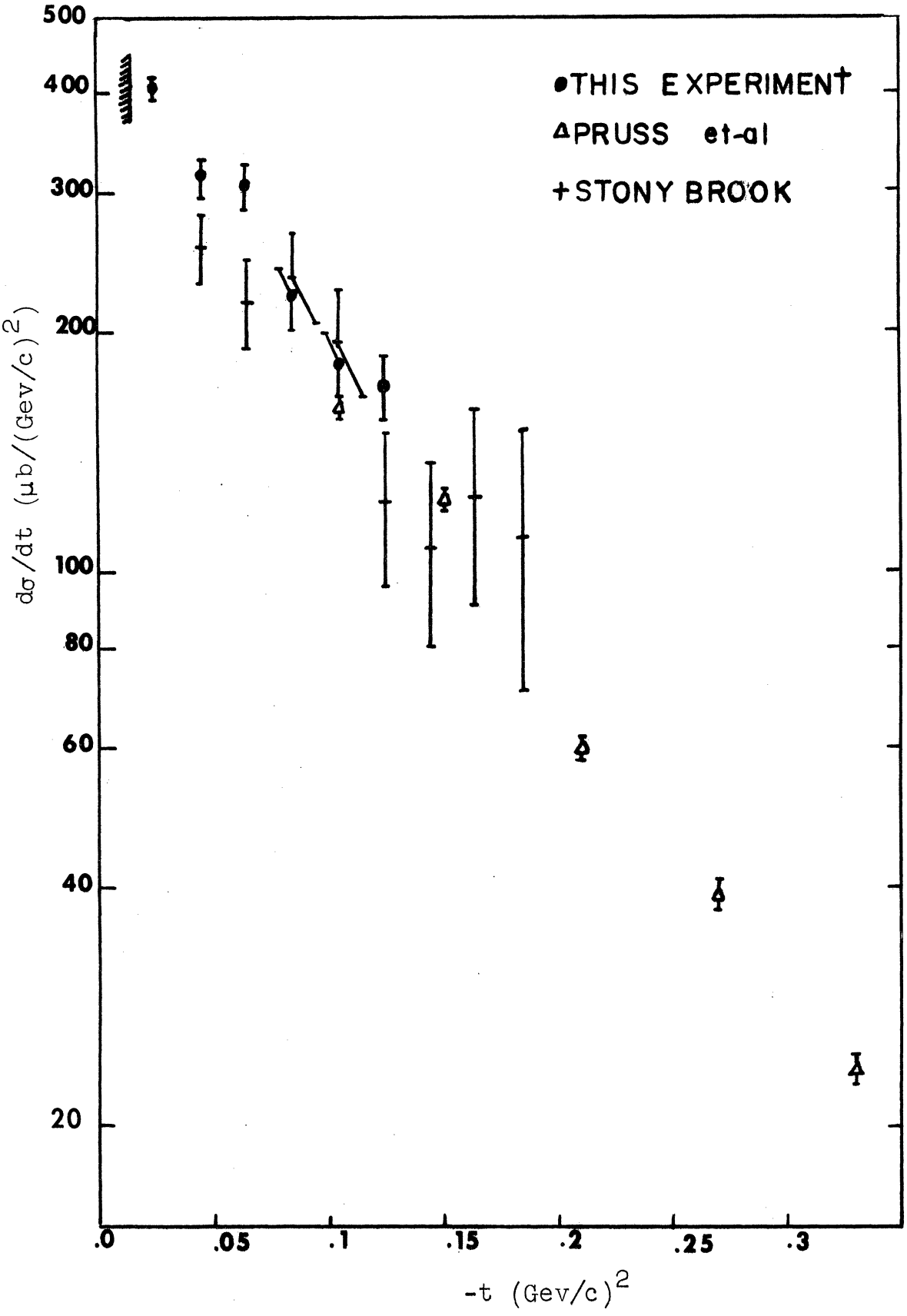

Figure 18. The comparison of this experiment on KΣ production at 5 Gev/c with others.

3.5 to 14. Gev/c. Figure 18 shows the results of this experiment at 5 Gev/c incident momenta, compared with the Stony Brook data at the same energy. The error bars in Figure 18 are statistical only. They also estimate 20% systematic errors. These two experiments agree within statistical and systematic errors.

B. Differential Cross Section for $\pi^+ + p \rightarrow K^+ + \Sigma^+$:

Figure 16 shows that the differential cross section for the reaction (5) at 5 and 7 Gev/c incident momenta, rises exponentially as $t \rightarrow t_{min}$ with slopes 9.37 and 9.01 $(Gev/c)^{-2}$, consistent with the previous experiment.[10] We observed no evidence for a forward dip and conclude as is explained in section D that there is no strong spin flip contribution to the differential cross section for this reaction.

The cross section for the reaction (5) at 3.0 Gev/c falls off more rapidly from t_{min} to $t \simeq -.1$ $(Gev/c)^2$ than at larger angles (Figure 16). It is possible that there is an s-channel effect interferring with t-channel exchange forces thereby giving a rapid rise to the cross section. The total energy in the center-of-mass system at 3 Gev/c is 2.56 Gev. There are several resonances near this energy, such as $\Delta(2420)$ and $\Delta(2850)$, which may decay into $K\Sigma$ and contribute to the cross section.

To investigate the possibility of such a interference, the Breit Wigner terms due to the resonance $(m=2420, J^p=(11/2)^+)$

were added to the t-channel amplitudes and the resulting expression for the cross section was fitted to the data. The cross section will be:[21,22]

$$\frac{d\sigma}{dt} = |f^s_{++} + f^t_{++}|^2 + |g^s_{+-} + g^t_{+-}|^2$$

where

$$f^s_{++} = \frac{1}{K}\sqrt{\frac{4\pi}{2\ell+1}}\ (\ell + 1)\ a_{\ell,\ell+1/2}\ Y^0_\ell\ (\Omega)$$

$$f^t_{++} = a\ e^{(b/2)t}\ e^{i\varphi_1}$$

$$g^s_{+-} = \frac{1}{K}\sqrt{\frac{4\pi}{2\ell+1}}\ \sqrt{\ell(\ell+1)}\ a_{\ell,\ell+1/2}\ Y^1_\ell\ (\Omega)$$

$$g^t_{+-} = \frac{c\sqrt{-t}}{2M}\ e^{(d/2)t}\ e^{i\varphi_2}$$

and

$$a_{\ell,\ell+1/2} = \frac{m\sqrt{\Gamma_e\Gamma_r}}{m^2 - s - im\Gamma}$$

Where m = 2420 Mev, Γ_e = 34.1 Mev, Γ = 310 Mev and Γ_r is not known. f_{++} and g_{+-} are the scattering spin flip and spin non-flip amplitudes. φ_1 and φ_2 are the phases between f^s_{++} and g^s_{+-} amplitudes and their corresponding Regge pole amplitudes, f^t_{++} and g^t_{+-}. (The details of the calculations and the definition of some of the parameters are given in Appendix I.) The solid line in Figure 19 shows the results of the least square fitting program. χ^2 (Chi-squared) was 22 for 7 degrees of freedom. One can note in Figure 19 that the very forward data points are all higher than the solid line making the fit a poor one. The spin flip and spin non-flip amplitudes and the slopes obtained from this fit were unrealistic in comparison to the corresponding

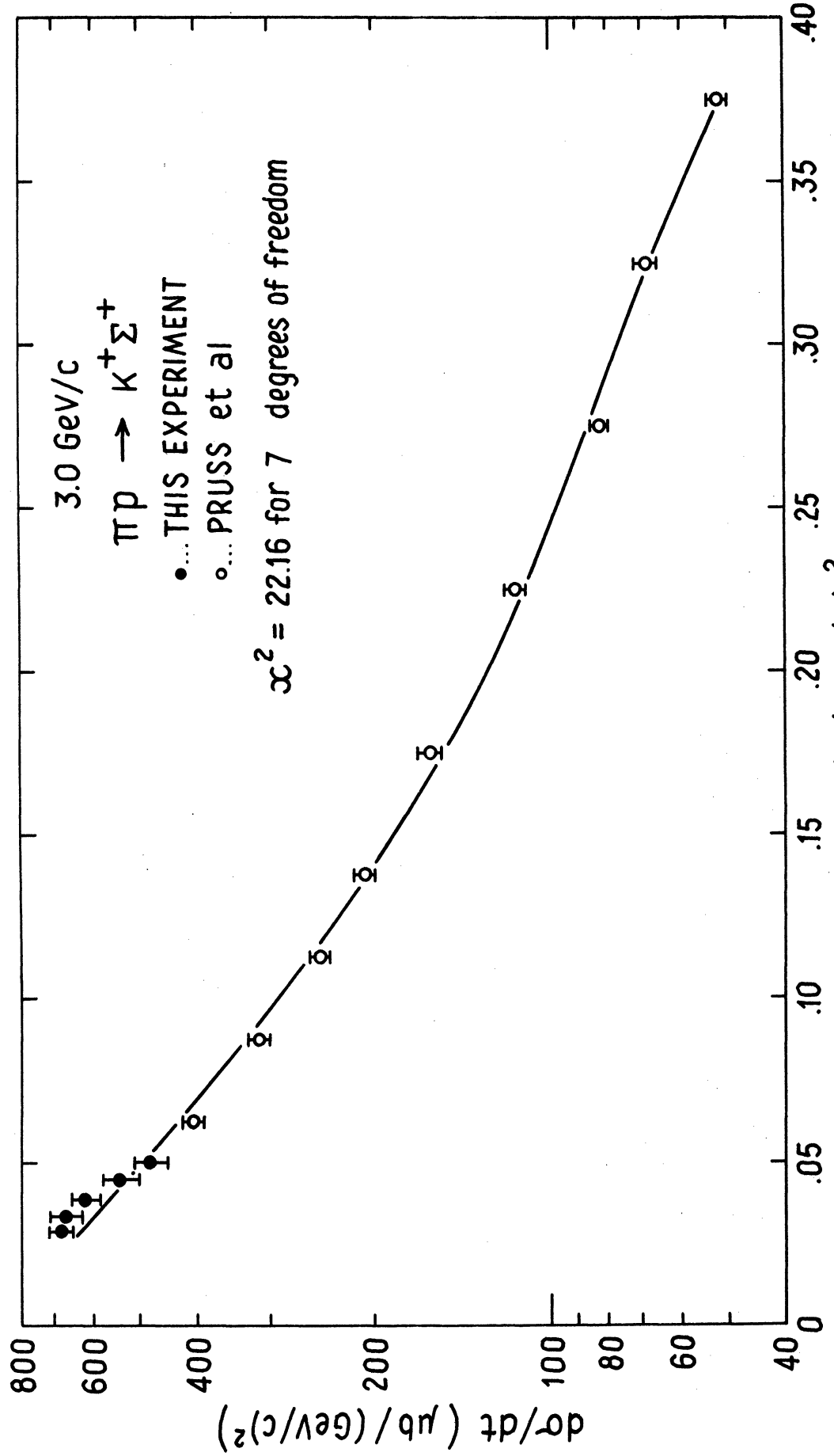

Figure 19. The results of the least square fitting program.

amplitudes and slopes at higher energies. It is apparent therefore that the simple Regge amplitude plus this Breit Wigner term will not explain this phenomena. It is possible that the resonances with higher spins might fit better to the data, but there is no direct evidence that such resonances exist.

We will next compare the data with the Regge pole theory. The Regge pole theory has been used more extensively to explain high energy collisions of strongly interacting particles than any of the other theoretical models.[4,23]

One of the several Regge pole models for hypercharge exchange reactions is the double Regge pole exchange of Reeder and Sarma.[24,25] This model is expected to be applicable to the forward direction. In this model the exchanges of $K^*(890)$ and $K^{**}(1420)$ trajectories are assumed for reaction (5). They assume exchange non-degeneracy because the SU(3) symmetry is broken, i.e., the masses in a given multiplet are not degenerate. K^* and K^{**} trajectories are obtained from ρ and A_2 trajectories by taking into account the SU(3) breaking. There are fourteen parameters in their model to be found from experimental data. These parameters are four residue constants, four energy scale factors, one 'cross over' factor and five parameters to define the K^* and K^{**} trajectories.

Figure 20, 21 and 22 show the results of the Reeder and Sarma model compared with the data of this experiment. As is shown in Figure 21 and 22, there is a good agreement between this model and experimental data at 5 and 7 Gev/c, but there

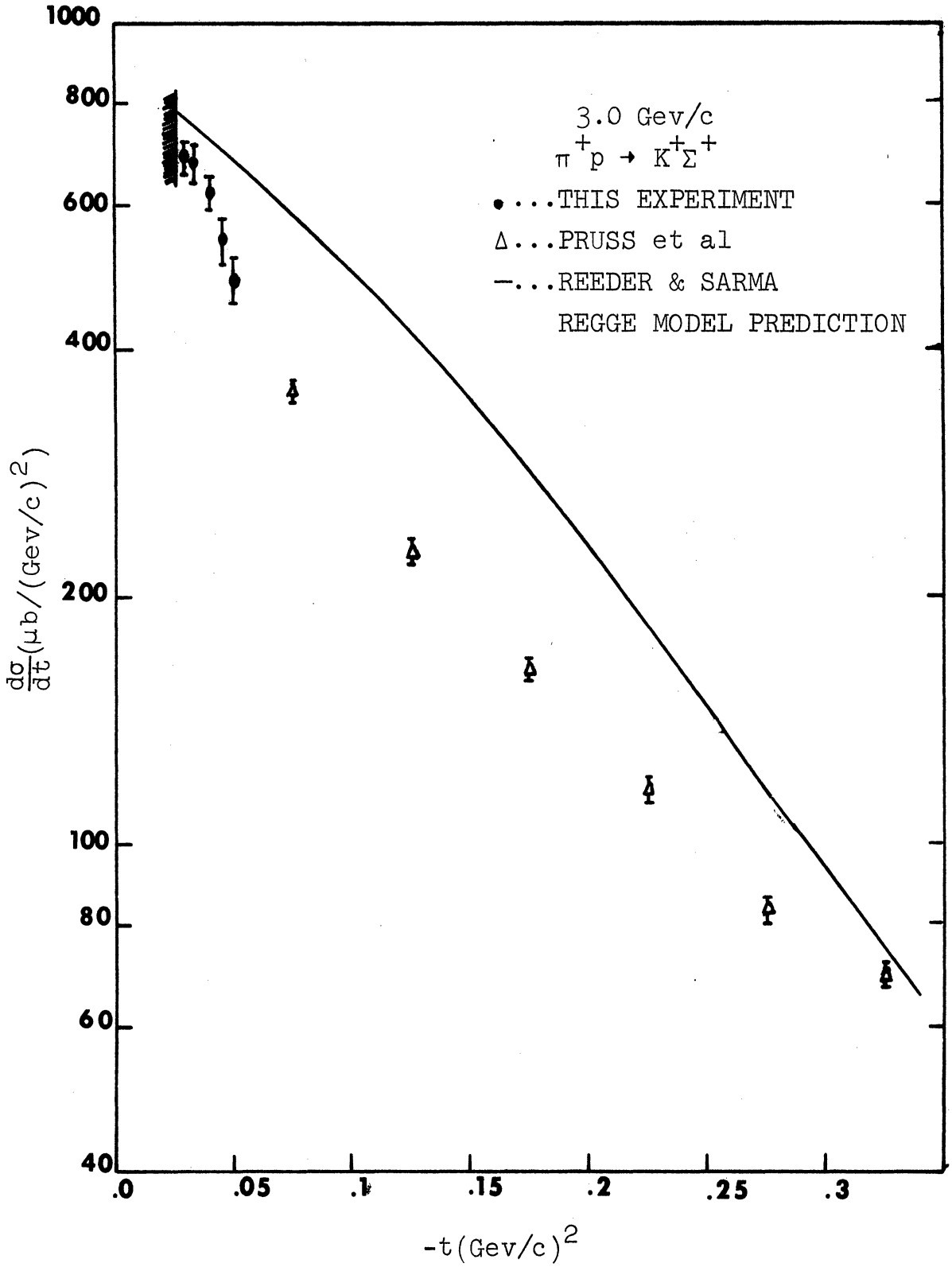

Figure 20. The comparison of the $\pi p \rightarrow K\Sigma$ cross section data with the Regge pole model

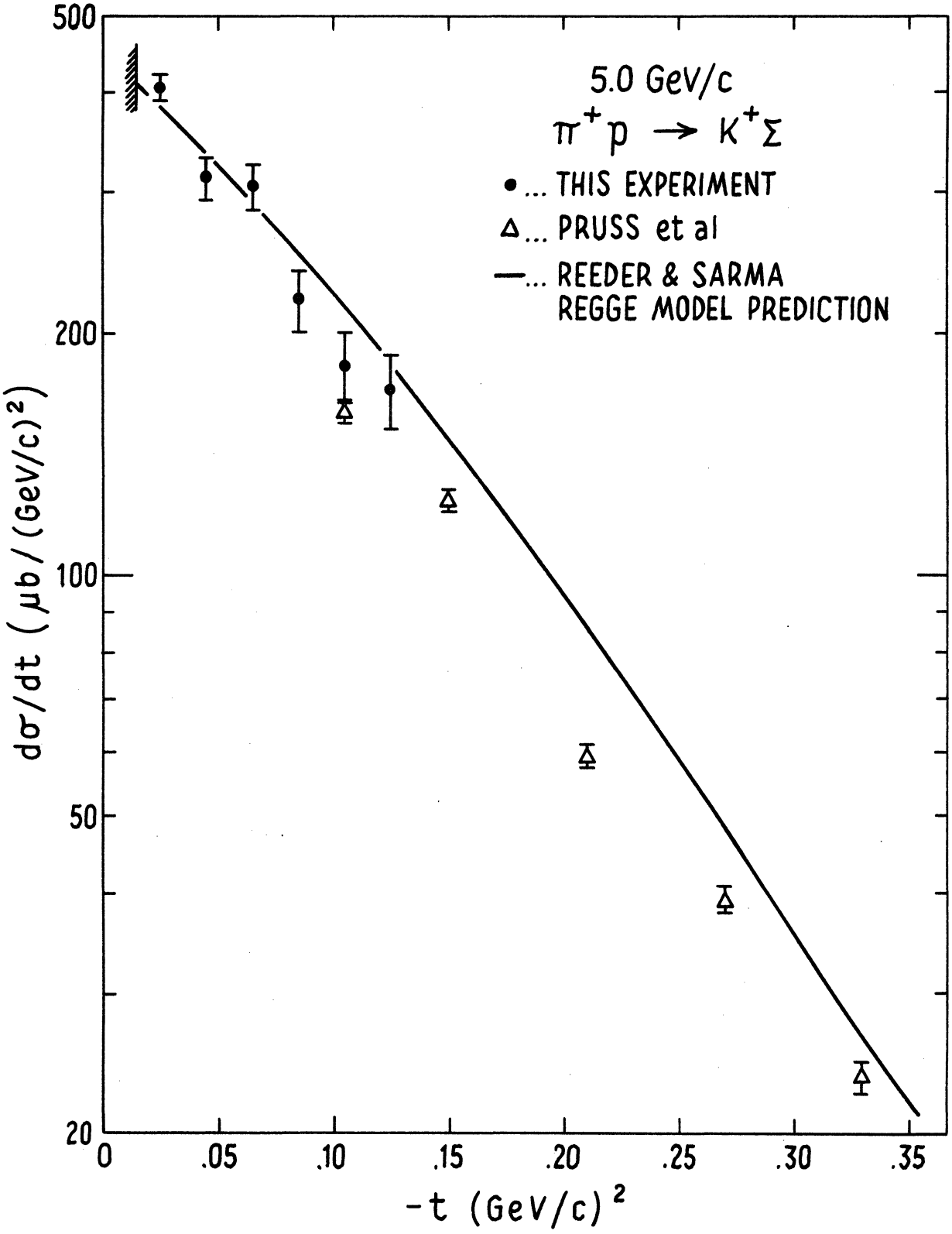

Figure 21. The comparison of the $\pi p \rightarrow K\Sigma$ cross section data with the Regge pole model.

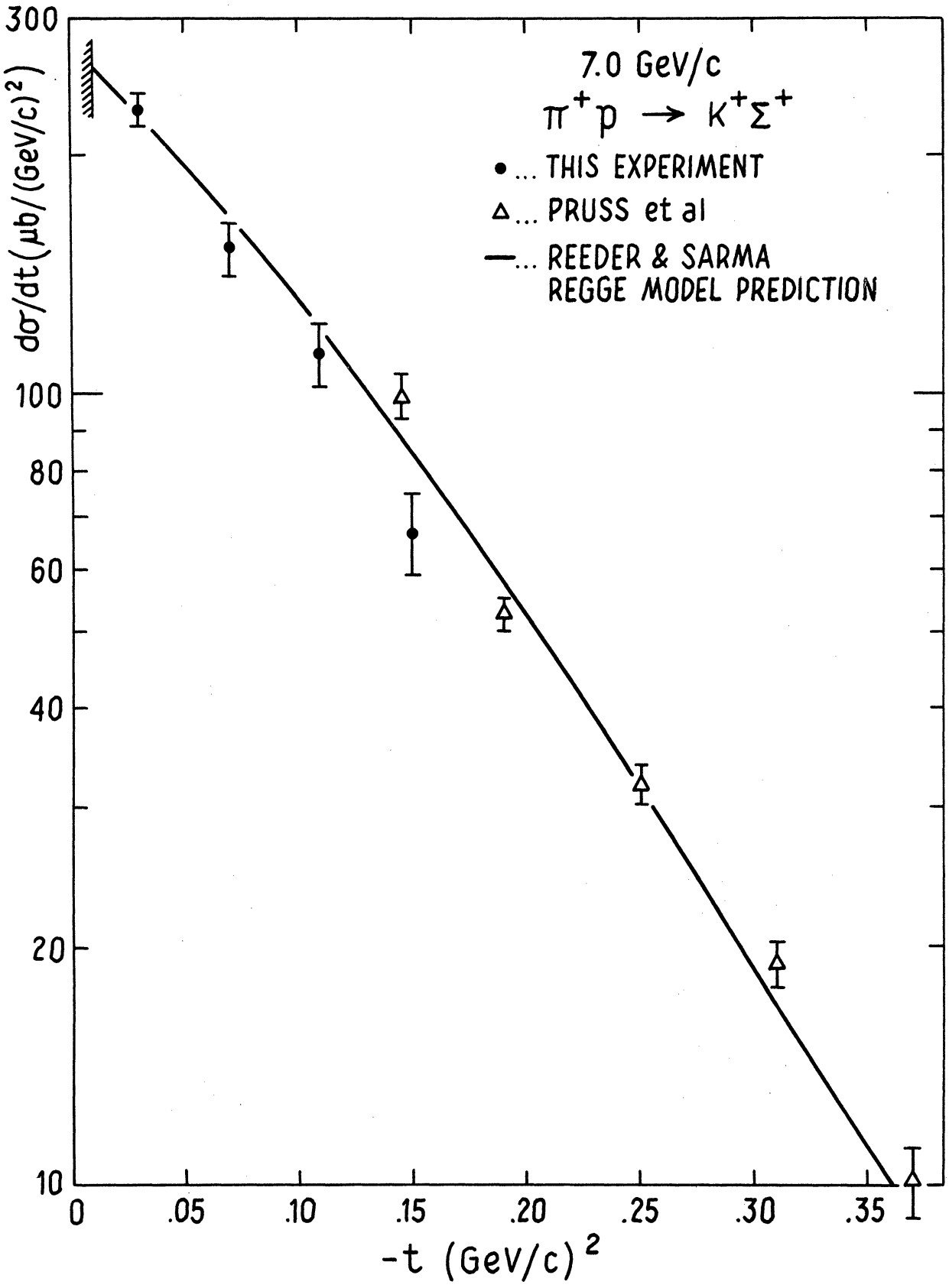

Figure 22. The comparison of the $\pi p \rightarrow K\Sigma$ cross section data with the Regge pole model.

is large disagreement at 3 Gev/c. It should be mentioned that this model also has some limitations not apparent from Figures 20 through 22. The model wildly disagrees with experimental data for $-t > 1.5$ $(Gev/c)^2$.

C. Differential Cross Section for $\pi^+ + p \rightarrow K^+ + Y^*(1385)$:

We also studied the reaction $\pi^+ + p \rightarrow K^+ + Y^*$ for which the exchanged trajectories in the t-channel are also K^* and K^{**}. But in this reaction the produced baryon, Y^*, belongs to the SU(3) decuplet while the Σ in the reaction (5) belongs to the SU(3) octet.

Figure 17 shows the results of this experiment on the reaction $\pi^+ + p \rightarrow K^+ + Y^*$ together with the previous measurements at larger angles.[13] There is a good agreement between these two experiments.

The remarkable feature of the reaction (6) is the turnover of the cross section in the forward direction, which is not seen in the reaction (5). Although the exchanged trajectories for both these reactions are the same, the amplitudes, slopes and the form of the cross sections are different. This turnover in the forward direction indicates that the cross section for the reaction (6) is strongly dominated by the spin flip amplitudes.

The differential cross section measured for the reaction (6) at 3.7[26] and 8 Gev/c[27] by other groups also show a

turnover near $t \simeq t_{min}$. Figure 23 shows the results of this experiment compared to others.

The turnover near zero degrees can be understood by the Stodolsky-Sakurai " ρ-photon analogy " hypothesis.[28] To understand this analogy intuitively, consider the electroproduction of a single pion via a virtual photon exchanged (Figure 24a):

$$e^- + p \rightarrow e^- + p + \pi^o \qquad (13)$$

The overall matrix element for the reaction (13) is proportional to the transition matrix element at the baryon vertex, i.e., for the process (Figure 24b).

$$\gamma + p \rightarrow \Delta_{3/2} \rightarrow p + \pi^o \qquad (14)$$

A multipole expansion of the transition matrix element,[29,30] at the baryon vertex, has shown that the process (14) is dominated by the magnetic moment (M1) transition,[28,31] which goes to zero at zero degrees. The experimental angular distribution of the photoproduction reaction (14) is in excellent agreement with that expected for a pure M1 transition.[32-35] Stodolsky and Sakurai suggest that the following processes (Figure 29c)

$$\pi^+ + p \rightarrow \Delta^{++}_{3/2}(1236) + \pi^o \qquad (15)$$

$$K^+ + p \rightarrow \Delta^{++}_{3/2}(1236) + K^o \qquad (16),$$

for which the exchanged particle is a $\rho(m=765, J^p=1^-)$ meson, are similar to the electroproduction of a sigle pion. They assume that the transition matrix element for the process (Figure 24d)

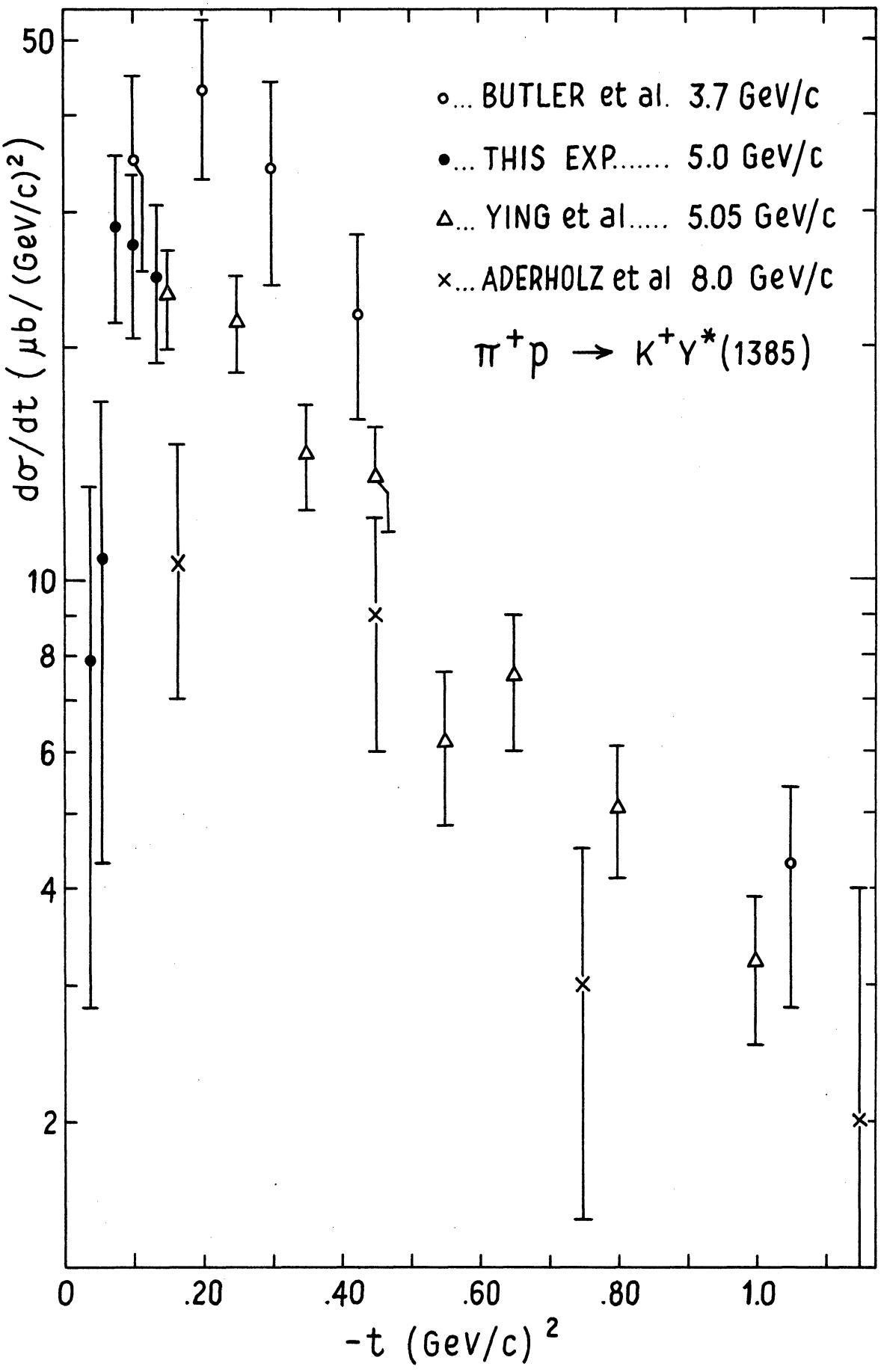

Figure 23. Comparison of this experiment with others on Y^*

$e^- + p \rightarrow e^- + p + \pi^o$

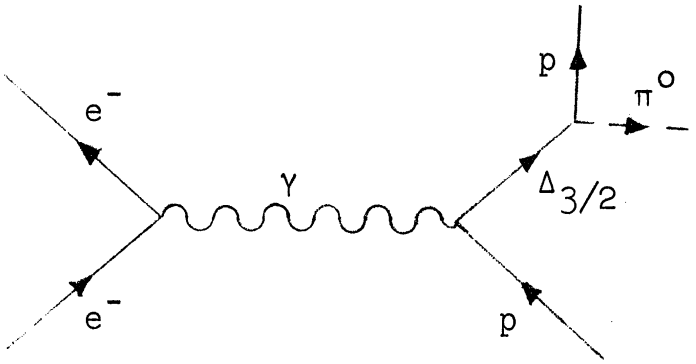

(a)

$\gamma + p \rightarrow \Delta_{3/2} \rightarrow p + \pi^o$

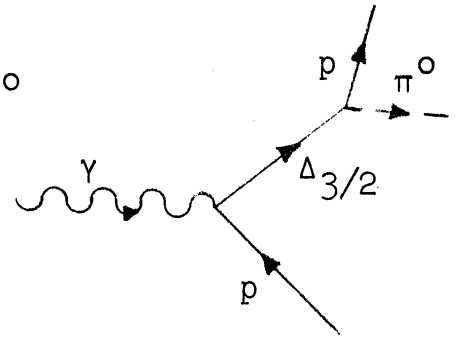

(b)

$\pi^+(K^+) + p \rightarrow \Delta^{++}(1236) + \pi^o(K^o)$

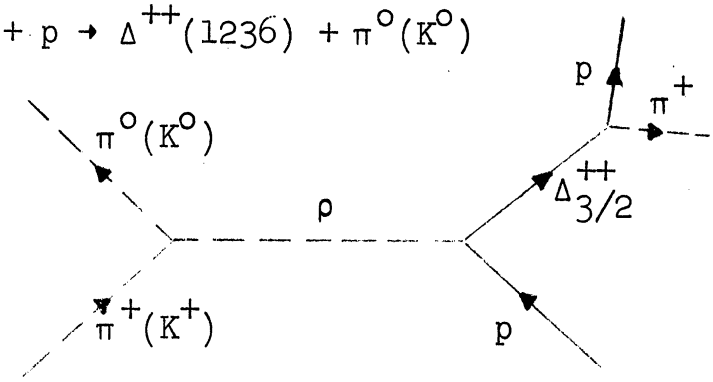

(c)

$\rho + p \rightarrow \Delta^{++}(1236) \rightarrow p + \pi^+$

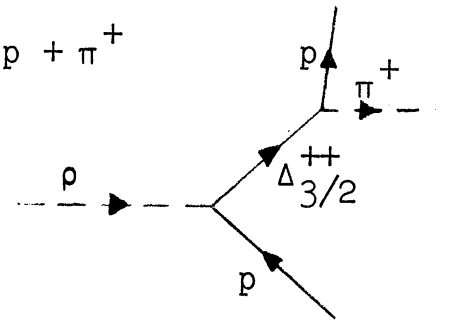

(d)

Figure 24. The Feynman diagrams for the isobar productions.

$$\rho^+ + p \rightarrow \Delta^{++}(1236) \rightarrow p + \pi^+ \qquad (17)$$

is proportional to the transition matrix elements for the photoproduction reaction (14). Because of this " ρ-photon analogy " it is natural to assume that the reactions (15) and (16) also go predominately via the magnetic moment (M1). The reactions (15) and (16) show a turnover near the forward direction,[36,37] which supports the idea of " ρ-photon analogy ".

Using the SU(3) symmetry which groups (Δ^{++}, Y^*), (π, K) and (ρ, K^*) into the same SU(3) multiplets,[38-42] we may speculate that the following processes:

$$\pi^+ + p \rightarrow K^+ + Y^* \qquad (18)$$

$$K^- + p \rightarrow \pi^- + Y^* \qquad (19)$$

also go predominately via magnetic transition (M1). The reaction (19) also shows a turnover near zero degree.[43,27]

A Regge pole analysis is done by Renninger and Sarma[45,46] to explain the isobar productions, $\Delta(1236)$ and $Y^*(1385)$, cross sections. The assumptions in this model are similar to the case of the $K\Sigma$ production, which is explained in the previous section. To explain the turnover in the forward direction, they have chosen the structure of the Regge residues to reflect the dominance of the magnetic dipole (M1) transition between the nucleon and the isobar. Figure 25 shows the predictions of this model for the KY^* production at 6 Gev/c compared with the data of the Stony-Brook at 6 Gev/c and the data of this experiment at 5. Gev/c.

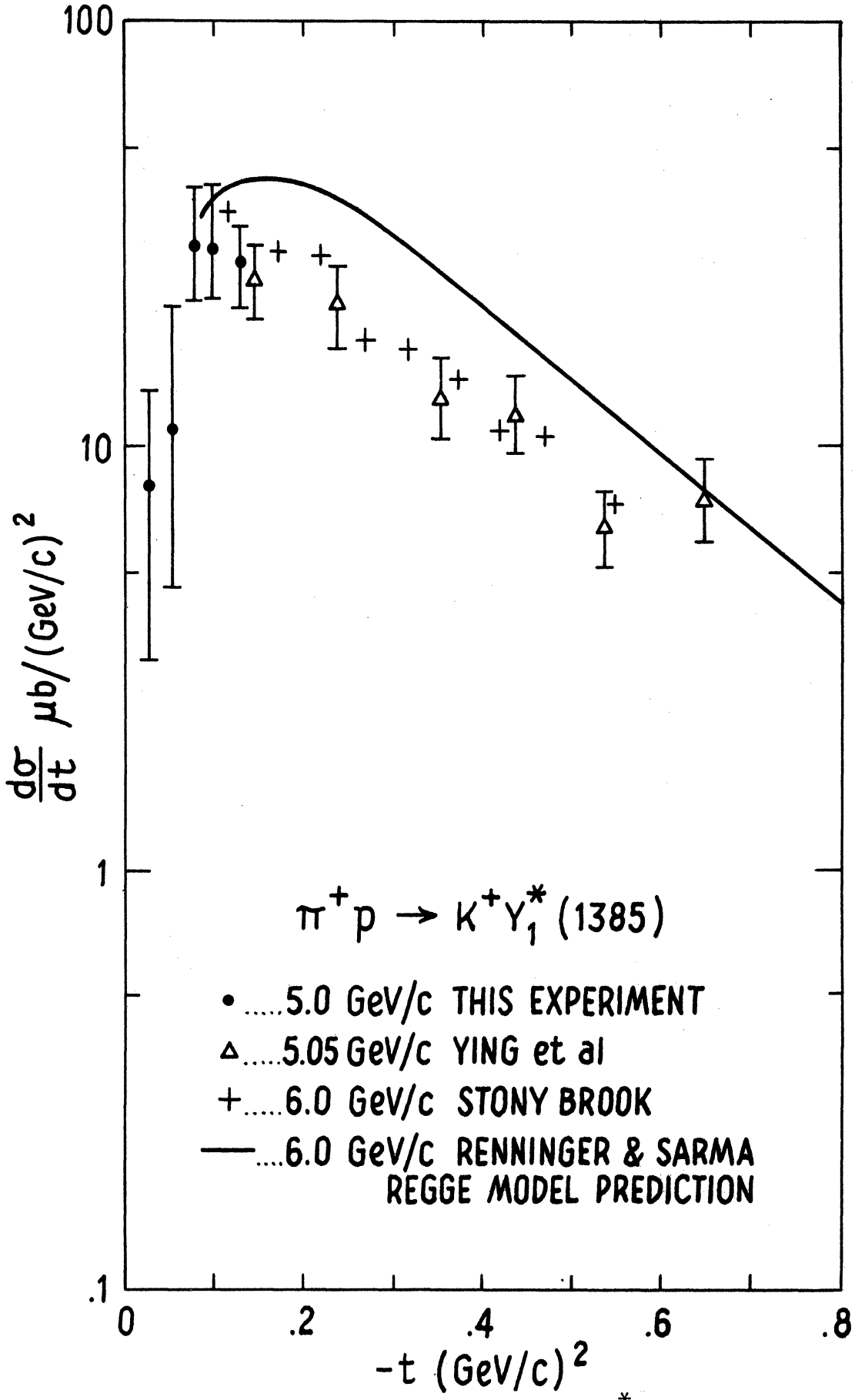

Figure 25. The comparison of the $\pi p \rightarrow KY^*$ cross section data with the Regge pole model.

As is shown in the Figure 25, this model explains the form of the cross section but its normalization is higher than this experiment.

D. Determination of the Helicity Flip and Non-Flip Amplitude:

In previous sections we concluded that the turnover of the cross section for the reaction $\pi p \rightarrow KY^*$ is due to the dominance of the helicity flip amplitudes over the helicity non-flip amplitude. We also stated that there is no strong helicity flip contribution to the reaction $\pi\ p \rightarrow K\ \Sigma$. We fitted the cross sections for the reactions (5) and (6) to the following function to find the contribution of the helicity flip and non-flip amplitudes in the cross section.

$$\frac{d\sigma}{dt} = \left[|A_{nf}|^2 + \frac{|t'|}{4M^2} |A_f|^2 \right] e^{-Bt'} \qquad (20)$$

where A_{nf} represents helicity non-flip and A_f represents helicity flip amplitudes, $t' = t - t_{min}$ and M is the mass of the proton. In equation (20) the term $\frac{|t'|^2}{16M^4} |A_{df}|^2$ which is due to the double helicity flip amplitude (a change of two units of the helicity, $T_{1/2} \rightarrow -3/2$) for the Y^* production was neglected because t' was small. The results of the least squared fitting are summarized in Table IV. For comparison the data for the charge exchange reaction[7-9] $\pi^- p \rightarrow \pi^0 n$ was similarly fitted to the equation (20).

We integrated the terms in equation (20) corresponding to the helicity flip and non-flip amplitudes over the interval $-t_{min} \leq -t \leq .4\ (Gev/c)^2$ for better understanding

	$\pi^+ + p \rightarrow K^+ + \Sigma^+$		$\pi^+ + p \rightarrow K^+ + Y^*$	$\pi^- + p \rightarrow \pi^\circ + n$
	5.0 Gev/c	7.0 Gev/c	5.0 Gev/c	4.83 Gev/c
A_{nf}	20.3 ± 0.3	16.4 ± 0.4	3.03 ± 0.75	21.4 ± 1.5
A_f	0.0 ± 35.0	$40.0 \begin{smallmatrix} + 20.0 \\ - 40.0 \end{smallmatrix}$	35.67 ± 5.33	192 ± 20.0
B	9.4 ± 0.8	10.3 ± 1.1	6.4 ± 1.0	12.0 ± 0.6
A_f/A_{nf}	0.0 ± 1.72	$2.44 \begin{smallmatrix} + 1.23 \\ - 2.49 \end{smallmatrix}$	11.77 ± 3.4	8.97 ± 1.12
$\frac{\sigma_f}{\sigma_{nf}}$	$0.0 \begin{smallmatrix} + 0.08 \\ - 0.0 \end{smallmatrix}$	$0.15 \begin{smallmatrix} + 0.19 \\ - 0.15 \end{smallmatrix}$	4.8 ± 2.8	1.8 ± 0.5

Table IV. The results of the best least squares fit to the equation 20.

of the contributions of these two amplitudes to the cross section. The integrated cross sections corresponding to the flip and non-flip terms are shown by σ_f and σ_{nf} in the Table IV. As is shown in Table IV the ratio of σ_f/σ_{nf} is consistent with zero for $K\Sigma$ data at 5 and 7 Gev/c. However, this ratio for KY^* data is 4.8 ± 2.8 and for $\pi^o n$ is $1.8 \pm .5$. Therefore, the cross section for KY^* production is dominated by the helicity flip amplitudes while $K\Sigma$ production is dominated by the helicity non-flip amplitude.

APPENDIX I

INTERFERENCE BETWEEN THE T-CHANNEL AND THE S-CHANNEL RESONANCE.

The very forward peak of the cross section for the reaction $\pi^+ p \rightarrow K^+ \Sigma$, at 3 Gev/c incident momenta, made us suspect that there probably is an s-channel effect interfering with t-channel. The total center-of-mass energy for the reaction $\pi p \rightarrow K\Sigma$ at 3 Gev/c incident pion momenta is 2.56 Gev/c. There are several resonances such as $\Delta(m = 2420\ J^P = \frac{11^+}{2})$ and $\Delta(m = 2850\ J^P = ?^+)$ which might decay to $K\Sigma$ and contribute to the cross section.

The following shows how the s-channel effect was calculated for the resonance $\Delta(2420)$. The scattering spin-flip and spin non-flip amplitudes resulting from a phase shift analysis are,

$$f(\theta) = \frac{1}{K} \sum_{\ell} \sqrt{\frac{4\pi}{2\ell+1}} \left[(\ell + 1)\, a_{\ell,\, j_+} + \ell\, a_{\ell,\, j_-} \right] Y_\ell^0 (\Omega)$$

$$g(\theta,\varphi) = \frac{1}{K} \sum_{\ell} \sqrt{\frac{4\pi}{2\ell+1}} \sqrt{\ell(\ell + 1)} \left[a_{\ell,\, j_+} - a_{\ell,\, j_-} \right] Y_\ell^{2m_s} (\Omega)$$

where K is the center-of-mass momenta of the particles in the initial state, $Y_\ell^m(\Omega)$ are the spherical harmonics and $a_{\ell,\, j_+}$ and $a_{\ell,\, j_-}$ are the partial wave scattering amplitudes for $j_\pm = \ell \pm 1/2$ respectively. From the conservation of parity for the transition $\pi p \rightarrow \Delta(2420)$ we obtain $\ell = 5$ and

$j = \ell + 1/2$. Therefore:

$$f(\theta) = \frac{1}{K}\sqrt{\frac{4\pi}{2\ell+1}}\ (\ell + 1)\ a_{\ell,\ \ell + 1/2}\ Y_\ell^o(\Omega)$$

$$g(\theta,\varphi) = \frac{1}{K}\sqrt{\frac{4\pi}{2\ell+1}}\ \sqrt{\ell(\ell + 1)}\ \ a_{\ell,\ \ell + 1/2}\ Y_\ell^1(\Omega)$$

We have

$$Y_\ell^m(\theta,\varphi) = \sqrt{\frac{2\ell+1}{4\pi}} \cdot \frac{(\ell - m)!}{(\ell + m)!}\ P_\ell^m\ (\cos\ \theta)\ e^{im\varphi}$$

where

$$P_\ell^m\ (\cos\ \theta) = \frac{(-1)^m}{2^\ell\ \ell!}\ (1 - x^2)^{\frac{m}{2}}\ \ \frac{d^{\ell + m}}{dx^{\ell + m}}\ (x^2 - 1)^\ell$$

where

$$x = \cos\ \theta.$$

From azimuthal symmetry of the scattering we can write

$$\varphi = 0.$$

The spherical harmonic functions for $\ell = 5$, $m = 0$ and $m = 1$ are

$$Y_5^o = \sqrt{\frac{11}{4\pi}}\ \left[\frac{1}{8}\ (63\ \cos^5\ \theta - 70\ \cos^3\ \theta + 15\ \cos\ \theta)\right]$$

$$Y_5^1 = \sqrt{\frac{11}{120\pi}}\ \left[-\frac{1}{8}\ (315\ \cos^4\ \theta - 210\ \cos^2\ \theta + 15)\ \ \sin\ \theta\right]$$

The partial wave amplitude $a_{\ell,\ \ell + 1/2}$ is

$$a_{\ell,\ \ell + 1/2} = \frac{m\sqrt{\Gamma_e \Gamma_r}}{m^2 - s - im\Gamma}$$

where m = 2420 Mev, Γ_e = 34.1 Mev and Γ_r is the width of the Δ resonance which is not known. Γ is the sum of all possible Γ_i's.

The central mass momentum, K, of the particles in the initial state is

$$K = \frac{[s - (m_\pi + m_p)^2]\,[s - (m_\pi - m_p)^2]}{4s}$$

Therefore the cross section is:

$$\frac{d\sigma}{dt} = \left| f(\theta) + ae^{\frac{b}{2}t}\ e^{i\varphi_1} \right|^2$$

$$+ \left| g(\theta,\varphi) + \frac{c\sqrt{-t}}{2m_p}\ e^{\frac{d}{2}t}\ e^{i\varphi_2} \right|^2$$

where φ_1 and φ_2 are the phases between the corresponding t- and s-channel scattering amplitudes. There are seven free parameters a, b, φ_1, c, d, φ_2 and Γ_r to be determined from a least square fitting of the above cross section to the measured cross section.

APPENDIX II. THE HIGH VOLTAGE PULSER

A fast rise time high voltage pulser with thyratron tubes was designed by Dr. Dave Rust at Argonne National Laboratory. Figure 26 shows the schematic diagram for the power supply of the thyratron and interlock unit to start the thyratron. The EVENT signal after being amplified from -.5 volts to -6 volts was sent to an avalanche driver; the schematic diagram of avalanche driver is shown in Figure 27. The output voltage of the avalanche driver at the points (1) and (2) were about 350 volts. The reason for having two circuits for avalanching rather than one is to make the delay time shorter. The outputs of the avalanche driver, points (1) and (2), were connected to a ferrite core (Figure 28) which combined the voltages and the resultant voltage was about 750 volts. This voltage was applied to one of the grids of the thyratron and the other grid was at a potential of 150 volts. A high voltage of about 6 kilovolts was applied to the anode of the thyratron through a diode. This thyratron pulser had a 50 nanoseconds rise time and a repetition rate of 300/second. One hundred volts was applied constantly on the chambers as a clearing field.

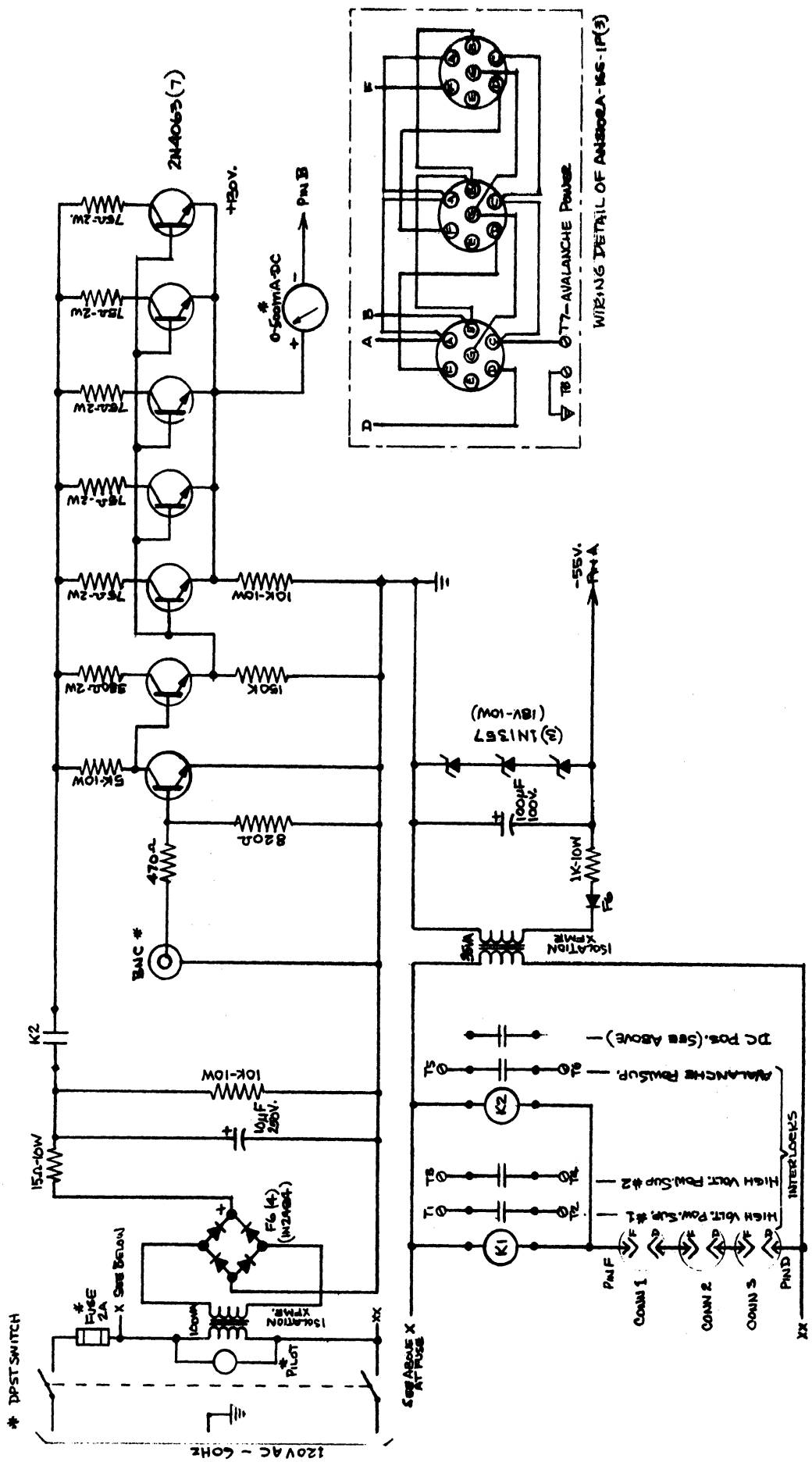

Figure 26. Thyratron pulser power supply.

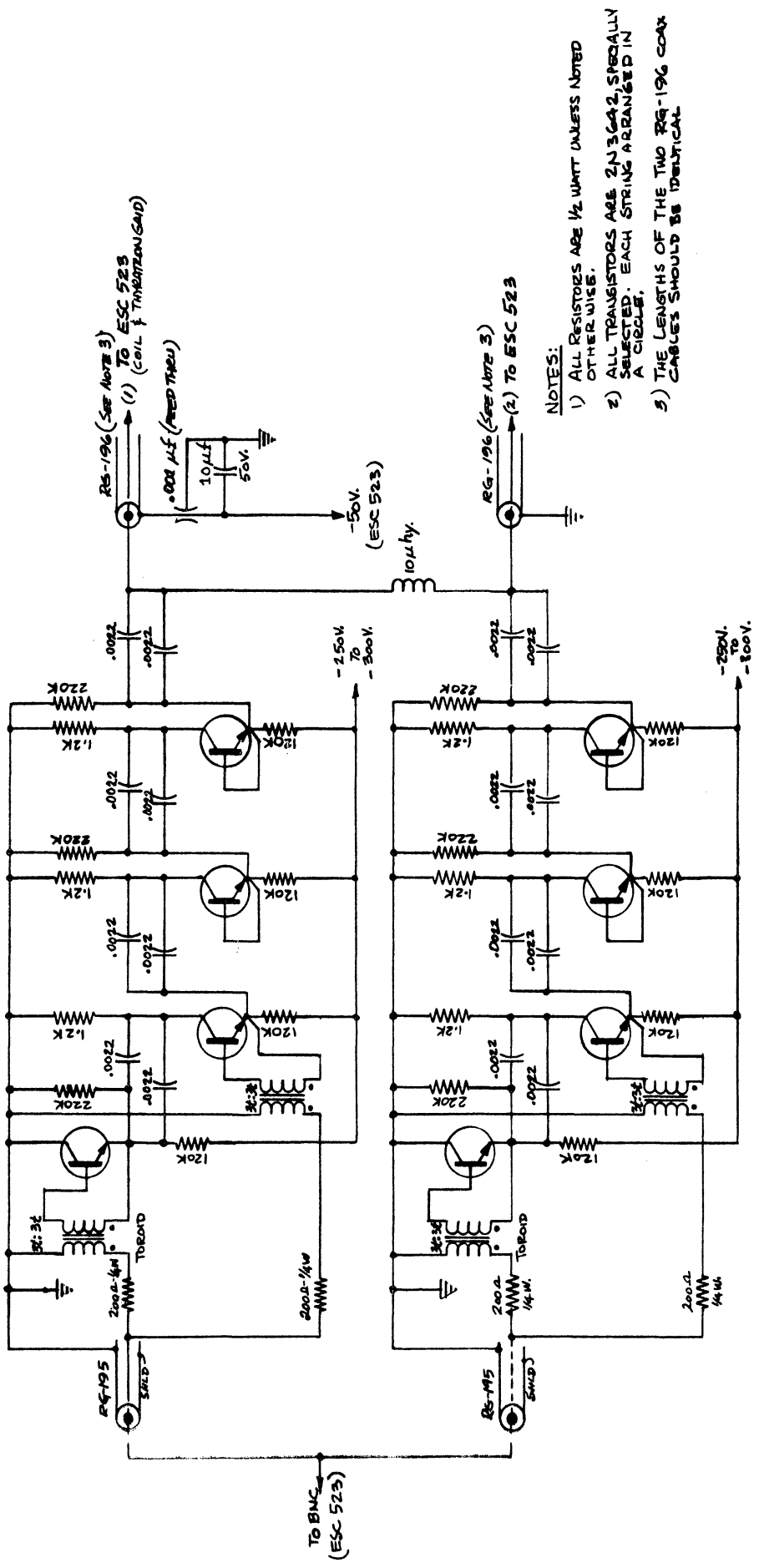

Figure 27. Avalanche driver.

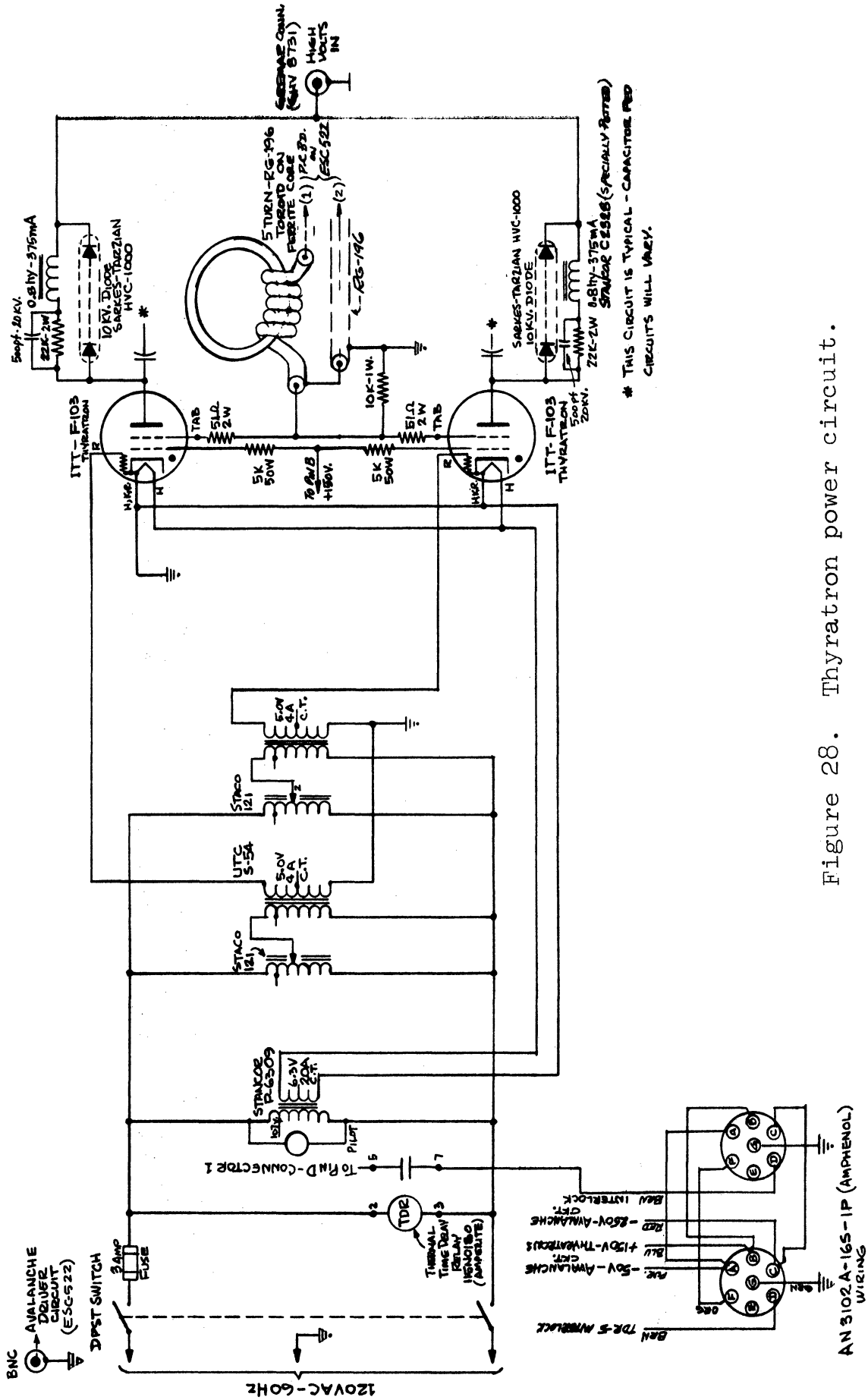

Figure 28. Thyratron power circuit.

APPENDIX III

NUCLEAR INTERACTION CORRECTION

The nuclear interaction correction depends on the total cross section σ_T. There are no measured cross sections (σ_T) of elementary particles on most of the nuclei that the material in our spectrometer consisted of. The only experimental data which exists on the σ_T for various nuclei are for pions and protons on a small number of nuclei[46-49]; cross sections for kaon on nuclei are almost non-existant. However, there is extensive experimental information on the total cross section, $\bar{\sigma}$,[4,21] for $\pi^{\pm}$, $K^{\pm}$, p and $\bar{p}$ on protons. The cross section, $\bar{\sigma}$, can be used to evaluate the total cross section on various nuclei by employing a theoretical model (an optical model). In the following, we give a brief survey of the theoretical calculation and then use two models, uniform density and Wood-Saxon, to calculate the cross sections for various nuclei. We tested the validity of these models by comparing the results obtained from these calculations with the existing experimental data on the total cross section for pions and protons on various nuclei. At the end of this appendix we present a table of cross sections, based on these two models, for various nuclei.

The scattering amplitude from a phase shift analysis is

$$f(\theta) = \sum_{\ell=0}^{\infty} (2\ell + 1)\, a_\ell P_\ell (\cos\theta) \qquad \text{(III.1)}$$

if spins of the particles are ignored. The partial wave scattering amplitudes, a_ℓ, in terms of the phase shifts are

$$a_\ell = \frac{e^{2i(\delta_\ell + i\,\chi_\ell/2)} - 1}{2iK} \qquad \text{(III.2)}$$

where K is the center-of-mass momenta of the particles in the initial states. $\chi_\ell/2$ is the imaginary part of the phase shift which leads to the absorption and δ_ℓ is the real part. One calculates the integrated cross sections to be[14]

$$\sigma_{\text{Total}} = \sigma_T = \frac{2\pi}{K^2} \sum_\ell (2\ell + 1)\left[1 - \cos 2\delta_\ell \; e^{-\chi_\ell}\right] \qquad \text{(III.3a)}$$

$$\sigma_{\text{absorption}} = \sigma_a = \frac{\pi}{K^2} \sum_\ell (2\ell + 1)\left[1 - e^{-2\chi_\ell}\right] \qquad \text{(III.3b)}$$

$$\sigma_{\text{elastic}} = \sigma_e = \frac{\pi}{K^2} \sum_\ell (2\ell + 1)\left[1 - 2\cos 2\delta_\ell e^{-\chi_\ell} + e^{-2\chi_\ell}\right] \qquad \text{(III.3c)}$$

Let

$$\ell = bK$$

where b is the impact parameter. For high energy scattering very large values of ℓ can contribute to the cross section; therefore, the summation in equations (III.3) can be replaced by integrals over b:

$$\sigma_T = 4\pi \int_0^\infty bdb \ (1 - e^{-\chi(b)}) \qquad \text{(III.4a)}$$

$$\sigma_a = 2\pi \int_0^\infty bdb \ (1 - e^{-2\chi(b)}) \qquad \text{(III.4b)}$$

$$\sigma_{\text{diffration}} = \sigma_d = \sigma_e = 2\pi \int_0^\infty bdb \ (1 - e^{-\chi(b)})^2 \qquad \text{(III.4c)}$$

where it is assumed that $\delta_\ell = 0$, which means we have pure diffraction scattering. It is shown that a small value for δ_ℓ will not change the answer very much.

It is now necessary to calculate $\chi(b)$. $\chi(b)$ is given in terms of the density of nuclear matter $\rho(r)$ which is normalized so that;

$$\int \rho(r) \ 4\pi r^2 dr = A$$

where A is the atomic number of the corresponding nucleus and r is the radial distance from the center of the nucleus. $\chi(b)$ is given by the following relation:[51]

$$\chi(b) = \int_0^\infty \frac{rdr}{(r^2 - b^2)^{1/2}} \ \bar{\sigma} \ \rho(r)$$

where $\bar{\sigma}$ is the total cross section of the incident particle with proton. Therefore, it is necessary to know $\rho(r)$ for calculating the cross sections (equations III.4). There have been many assumptions for the form of the nuclear potential $\rho(r)$ to reproduce the experimental data. The

following are two of these assumptions for $\rho(r)$.

A. Square Well (Uniform density)

$$\rho(r) = \frac{3A}{4\pi R^3} \quad \text{for} \quad r < R$$

$$\rho(r) = 0 \quad \text{for} \quad r > R$$

where R is the radius of the nucleus. The integrals for the equations (III.4) can be calculated and the results are:

$$\sigma_T = 2\pi R^2 \left\{1 - \left[1 - \left(1 + \frac{\alpha R}{2}\right) e^{\frac{-\alpha R}{2}}\right] \frac{8}{(\alpha R)^2}\right\} \qquad \text{(III.5a)}$$

$$\sigma_a = \pi R^2 \left\{1 - \left[1 - \left(1 + \alpha R\right) e^{-\alpha R}\right] \frac{2}{(\alpha R)^2}\right\} \qquad \text{(III.5b)}$$

$$\sigma_d = \sigma_T - \sigma_a \qquad \text{(III.5c)}$$

where

$$\alpha = \frac{3\bar{\sigma}A}{2\pi R^3}$$

B. Wood-Saxon Potential

$$\rho = \frac{\rho_o}{e^{(r-c)/Z} + 1}$$

This potential has reproduced the experimental data more

successfully than any other potential. To calculate the nuclear interaction correction for our experiment, we used the total cross sections (σ_T) obtained from this model. The value of ρ_o can be determined from the normalization of $\rho(r)$ and from electron scattering we have

$$c = 1.08\ A^{1/3}\ \text{fermi}\ (= 10^{-13}\ \text{centimeter})$$

$$Z = .53\ \text{fermi}$$

while the hadron-nucleus cross sections yield

$$c = 1.13\ A^{1/3}\ \text{fermi}$$

The integrals in equations (III.4) can not be evaluated analytically for the Wood-Saxon potential, but they can be evaluated numerically.

A Fortran program was written to calculate the cross sections for both the square-well and the Wood-Saxon potential. It also included an empirical formula for the absorption cross section which is based on the optical model.[50]

$$\sigma_a = 44\ A^{0.69}\left[1 + .039\ A^{-1/3}\ (\bar{\sigma} - 33) - .0009\ A^{-1/3}(\bar{\sigma} - 33)^2\right]$$

Table V shows the comparison between the cross section calculation from the Wood-Saxon model and the experimental data.

Table V

Comparison of Wood-Saxon Model
With Experiment

23 Gev Proton Inelastic Data (Ashmore et al.)

Material	Data	$\sigma_a(\bar{\sigma} = 40mb)$
Be	180±5	219.3
C	225±5	270.4
Al	400±10	474.1
Cu	740±20	833.8
Sn	1221±26	1236.0
Pb	1750±30	1757.0

3 Gev π^+ (Longo and Moyer)

Material	Data		Calculation		
	σ_a	σ_d	σ_a	σ_d	$(\bar{\sigma} = 33mb)$
Be	192±8	41.5±3.5	192.7	41.6	
C	213±8	66.6±7	242.3	60.2	
Al	428±15	160 ±14	435.8	157.1	
Cu	790±41	445 ±60	784.7	385.2	

3 Gev p (Longo and Moyer)

Material	Data		Calculation		
	σ_a	σ_d	σ_a	σ_d	$(\bar{\sigma} = 44mb)$
Be	236±4	64.8±2.4	231.9	62.4	
C	260±6	107±6	284.6	88.2	
Al	503±16	236±17	492.7	214.0	
Cu	914±44	620±65	857.0	485.7	

Table V (cont'd)

3.0 Gev K^+ (Abrams et al.)

Material	Inelastic Data	σ_a ($\bar{\sigma}$ = 17 mb)
C	155±1.2	155.0
Cu	595±6	594.0

970 MeV π^- (Cronin et al.)

Material	Data		Calculation		($\bar{\sigma}$ = 33 mb)
	σ_a	σ_d	σ_d	σ_d	
Be	197±9	76±15	194.7	41.6	
C	252±13	78±21	242.3	60.2	
Al	442±20	217±41	435.8	157.1	
Cu	806±35	290±60	784.7	385.2	

We extended our calculation for many elements and covered values of $\bar{\sigma}$ which should be adequate for $\pi^{\pm}$, $K^{\pm}$, p, n and $\bar{p}$. The abbreviations used in the Table VI are

SIGBAR = $\bar{\sigma}$

SIGA = σ_a

SIGD = σ_d

SIGT = σ_T

SIGBAR = 17.0 MB
C = 1.13 A**1/3 F
Z = 0.53 F
RØ = 1.30 F

Table VI

MATERIAL	UNIFORM MODEL			WILLIAMS	WOOD-SAXON		
	SIGA	SIGD	SIGT	SIGA	SIGA	SIGD	SIGT
HE	52.0	7.2	59.2	52.9	59.0	4.2	63.2
LI	86.4	14.4	100.8	93.2	97.2	9.9	107.1
BE	108.2	19.5	127.8	118.1	120.9	14.4	135.3
C	139.8	27.7	167.5	153.2	154.7	21.7	176.4
N2	160.2	33.3	193.4	175.5	176.2	26.9	203.1
O2	180.1	39.0	219.1	197.0	197.0	32.3	229.3
F	209.3	47.8	257.1	228.1	227.1	40.8	267.8
NE	218.8	50.8	269.6	238.2	236.8	43.7	280.5
AL	283.5	72.1	355.6	305.9	302.2	64.6	366.7
CL	362.3	100.6	462.9	386.6	380.1	92.8	472.8
FE	524.8	166.3	691.1	549.5	536.3	158.2	694.5
CU	586.1	193.2	779.3	610.0	594.0	184.9	778.9
SN	970.0	381.7	1351.7	983.4	945.4	370.5	1315.9
W	1369.1	606.5	1975.6	1366.1	1298.5	586.9	1885.5
PB	1506.4	689.3	2195.6	1497.2	1418.0	665.3	2083.3
U	1672.0	792.3	2464.3	1655.3	1561.2	762.2	2323.4

SIGBAR = 20.0 MB
C = 1.13 A**1/3 F
Z = 0.53 F
RØ = 1.30 F

MATERIAL	UNIFORM MODEL			WILLIAMS	WOOD-SAXON		
	SIGA	SIGD	SIGT	SIGA	SIGA	SIGD	SIGT
HE	58.5	9.5	68.0	67.0	67.8	5.6	73.5
LI	96.5	18.8	115.3	110.4	110.7	13.2	123.8
BE	120.5	25.4	145.9	136.9	137.1	18.9	156.0
C	154.9	35.7	190.6	174.2	174.3	28.3	202.6
N2	177.1	42.8	219.8	197.5	197.8	34.9	232.7
O2	198.6	50.2	248.6	222.1	220.5	41.8	262.3
F	230.1	61.1	291.2	252.7	253.2	52.4	305.6
NE	240.4	64.8	305.2	263.2	263.8	56.0	319.8
AL	309.8	91.4	401.2	333.7	334.2	81.9	416.1
CL	393.8	126.5	520.3	417.4	417.4	116.4	533.8
FE	565.6	206.5	772.1	585.6	582.5	195.2	777.6
CU	630.0	238.9	868.9	647.9	643.1	226.9	869.9
SN	1030.0	462.6	1492.5	1030.6	1008.3	442.7	1451.0
W	1441.3	723.9	2165.2	1421.3	1371.5	688.0	2059.5
PB	1582.1	818.9	2401.1	1554.9	1493.8	775.7	2269.5
U	1751.6	936.6	2688.2	1715.9	1640.1	883.4	2523.5

SIGBAR = 22.0 MB
C = 1.13 A**1/3 F
Z = 0.53 F
RØ = 1.30 F

Table VI (cont'd)

MATERIAL	UNIFORM MODEL			WILLIAMS	WOOD-SAXON		
	SIGA	SIGD	SIGT	SIGA	SIGA	SIGD	SIGT
HE	62.5	11.2	73.7	75.7	73.5	6.7	80.2
LI	102.6	21.9	124.5	121.1	119.2	15.5	134.6
BE	127.8	29.4	157.3	148.6	147.1	22.1	169.3
C	163.9	41.2	205.2	187.0	186.4	32.9	219.3
N2	187.1	49.3	236.4	211.2	211.1	40.5	251.6
O2	209.6	57.6	267.1	234.4	234.9	48.3	283.2
F	242.3	70.1	312.4	267.9	269.1	60.4	329.4
NE	253.0	74.3	327.3	278.8	280.1	64.4	344.6
AL	325.0	104.4	429.3	351.0	353.4	93.7	447.0
CL	411.8	143.9	555.5	436.6	439.4	132.2	571.7
FE	588.4	232.8	821.2	608.0	609.3	219.2	828.5
CU	654.4	268.6	923.0	671.4	671.3	254.0	925.3
SN	1062.1	513.7	1575.8	1059.9	1043.6	487.5	1531.1
W	1479.1	796.3	2275.3	1455.6	1411.8	749.1	2160.8
PB	1621.4	898.4	2519.8	1590.7	1535.5	841.8	2377.2
U	1792.5	1024.3	2816.8	1753.3	1683.3	955.3	2638.5

SIGBAR = 24.0 MB
C = 1.13 A**1/3 F
Z = 0.53 F
RØ = 1.30 F

MATERIAL	UNIFORM MODEL			WILLIAMS	WOOD-SAXON		
	SIGA	SIGD	SIGT	SIGA	SIGA	SIGD	SIGT
HE	66.3	12.8	79.1	83.9	79.0	7.8	86.7
LI	108.3	25.0	133.4	131.2	127.3	17.9	145.2
BE	134.6	33.6	168.2	159.6	156.7	25.5	182.2
C	172.1	46.9	219.1	199.1	197.8	37.7	235.5
N2	196.1	56.0	252.1	224.0	223.6	46.3	269.9
O2	219.5	65.2	284.7	247.9	248.4	55.0	303.4
F	253.3	79.2	332.6	282.3	283.9	68.5	352.4
NE	264.4	83.9	348.3	293.4	295.3	73.0	368.3
AL	338.5	117.3	455.8	367.2	371.0	105.4	476.4
CL	427.6	160.9	588.5	454.6	459.6	147.9	607.5
FE	608.2	258.5	866.7	629.1	633.4	242.6	876.0
CU	675.4	297.5	973.0	693.5	696.7	280.1	976.8
SN	1089.2	562.2	1651.4	1087.5	1074.7	529.7	1604.4
W	1510.3	863.8	2374.1	1487.8	1446.9	805.2	2252.1
PB	1653.8	972.1	2625.8	1624.3	1571.8	902.2	2473.9
U	1826.0	1105.3	2931.3	1788.6	1720.8	1020.5	2741.4

SIGBAR = 26.0 MB
C = 1.13 A**1/3 F
Z = 0.53 F
RO = 1.30 F

Table VI (cont'd)

MATERIAL	UNIFORM MODEL			WILLIAMS	WOOD-SAXON		
	SIGA	SIGD	SIGT	SIGA	SIGA	SIGD	SIGT
HE	69.8	14.6	84.4	91.6	84.3	8.9	93.2
LI	113.6	28.3	141.9	140.6	135.1	20.4	155.5
BE	140.9	37.8	178.7	169.8	165.9	28.9	194.8
C	179.7	52.6	232.3	210.5	208.7	42.6	251.3
N2	204.4	62.7	267.1	236.1	235.4	52.1	287.5
O2	228.5	72.9	301.3	260.5	261.1	61.8	322.9
F	263.3	88.3	351.6	295.7	297.7	76.6	374.4
NE	274.6	93.5	368.1	307.1	309.5	81.6	391.2
AL	350.6	130.1	480.8	382.5	387.3	117.1	504.5
CL	441.7	177.7	619.3	471.5	478.0	163.3	641.3
FE	625.5	283.4	908.9	648.8	655.2	265.2	920.4
CU	693.7	325.5	1019.2	714.2	719.5	305.3	1024.9
SN	1112.2	608.1	1720.3	1113.4	1102.4	569.1	1671.5
W	1536.4	926.5	2462.9	1518.0	1478.0	856.6	2334.6
PB	1680.6	1040.2	2720.8	1655.9	1603.8	957.3	2561.0
U	1853.7	1179.6	3033.3	1821.7	1753.9	1079.7	2833.6

SIGBAR = 28.0 MB
C = 1.13 A**1/3 F
Z = 0.53 F
RO = 1.30 F

MATERIAL	UNIFORM MODEL			WILLIAMS	WOOD-SAXON		
	SIGA	SIGD	SIGT	SIGA	SIGA	SIGD	SIGT
HE	73.1	16.4	89.5	98.8	89.4	10.2	99.6
LI	118.5	31.5	150.0	149.3	142.6	22.9	165.5
BE	146.6	42.1	188.8	179.4	174.6	32.5	207.0
C	186.6	58.4	245.0	221.2	218.9	47.6	266.5
N2	212.0	69.4	281.4	247.3	246.6	58.0	304.6
O2	236.6	80.6	317.2	272.3	273.0	68.6	341.6
F	272.3	97.4	369.7	308.2	310.6	84.8	395.5
NE	283.9	103.1	386.9	319.8	322.8	90.3	413.0
AL	361.5	142.8	524.3	396.7	402.4	128.8	531.2
CL	454.2	194.1	648.2	487.2	495.0	178.4	673.4
FE	640.6	307.4	948.0	667.2	675.1	287.0	962.1
CU	709.7	352.3	1061.9	733.6	740.3	329.5	1069.8
SN	1131.8	651.2	1783.0	1137.5	1127.2	605.9	1733.1
W	1558.3	984.5	2542.8	1546.1	1505.7	903.9	2409.5
PB	1723.1	1102.8	2805.9	1685.3	1632.3	1007.5	2639.8
U	1876.8	1247.6	3124.4	1852.6	1783.3	1133.4	2916.7

SIGBAR = 30.0 MB
C = 1.13 A**1/3 F
Z = 0.53 F
RØ = 1.30 F

Table VI (cont'd)

MATERIAL	UNIFORM MODEL			WILLIAMS	WOOD-SAXON		
	SIGA	SIGD	SIGT	SIGA	SIGA	SIGD	SIGT
HE	76.3	18.2	94.5	105.5	94.4	11.4	105.8
LI	123.0	34.9	157.9	157.5	149.8	25.6	175.4
BE	152.0	46.4	198.4	188.3	182.9	36.1	219.0
C	192.9	64.2	257.1	231.0	228.6	52.6	281.2
N2	218.9	76.1	295.0	257.7	257.0	64.0	321.0
O2	244.1	88.2	332.3	283.3	284.2	75.5	359.7
F	280.5	106.4	386.9	319.8	322.8	93.0	415.8
NE	292.3	112.5	404.7	331.6	335.1	98.9	434.1
AL	371.2	155.2	526.4	429.8	416.5	140.2	556.7
CL	465.2	210.1	675.3	501.8	510.7	193.2	703.8
FE	653.8	330.6	984.4	684.3	693.2	308.0	1001.2
CU	723.5	378.0	1101.5	751.5	759.2	352.6	1111.8
SN	1148.5	691.6	1840.1	1159.8	1149.6	640.3	1789.9
W	1576.7	1038.0	2614.7	1572.2	1530.6	947.1	2477.7
PB	1721.9	1160.4	2882.3	1712.6	1657.9	1053.4	2711.3
U	1896.0	1309.7	3205.8	1881.2	1809.8	1182.1	2991.8

SIGBAR = 32.0 MB
C = 1.13 A**1/3 F
Z = 0.53 F
RØ = 1.30 F

MATERIAL	UNIFORM MODEL			WILLIAMS	WOOD-SAXON		
	SIGA	SIGD	SIGT	SIGA	SIGA	SIGD	SIGT
HE	79.2	20.1	99.3	111.6	99.3	12.7	112.0
LI	127.3	38.2	165.5	165.0	156.7	28.3	185.0
BE	156.9	50.8	207.6	196.5	190.8	39.7	230.6
C	198.7	69.9	268.6	240.1	237.8	57.7	295.5
N2	225.2	82.8	308.0	267.3	267.0	70.0	336.9
O2	250.8	95.8	346.6	293.3	294.7	82.4	377.1
F	287.8	115.3	403.1	330.6	334.1	101.2	435.3
NE	299.8	121.8	421.6	342.6	346.8	107.5	454.2
AL	379.9	167.4	547.3	422.0	429.6	151.5	581.1
CL	475.1	225.6	700.7	515.3	525.2	207.6	732.7
FE	665.4	352.7	1018.1	700.1	709.9	328.0	1038.0
CU	735.7	402.5	1138.2	768.0	776.5	374.6	1151.1
SN	1162.9	729.4	1892.3	1180.4	1170.0	672.3	1842.3
W	1592.3	1087.3	2679.6	1596.3	1553.2	986.8	2540.0
PB	1737.8	1213.1	2951.0	1737.7	1681.2	1095.3	2776.4
U	1912.3	1366.4	3278.7	1907.6	1833.8	1226.3	3060.1

SIGBAR = 33.Ø MB
C = 1.13 A**1/3 F
Ƶ = Ø.53 F
RØ = 1.3Ø F

Table VI (cont'd)

MATERIAL	UNIFORM MODEL			WILLIAMS	WOOD-SAXON		
	SIGA	SIGD	SIGT	SIGA	SIGA	SIGD	SIGT
HE	8Ø.6	21.Ø	1Ø1.6	114.5	1Ø1.6	13.4	115.Ø
LI	129.3	39.9	169.2	16Ø.5	16Ø.Ø	29.7	189.7
BE	159.2	52.9	212.1	2ØØ.4	194.7	41.6	236.3
C	2Ø1.4	72.7	274.2	244.4	242.3	6Ø.2	3Ø2.5
N2	228.2	86.1	314.3	271.8	271.7	72.9	344.7
O2	254.Ø	99.5	353.5	298.1	299.8	85.8	385.6
F	291.3	119.6	41Ø.9	335.6	339.6	1Ø5.2	444.8
NE	3Ø3.4	126.4	429.7	347.7	352.3	111.7	464.Ø
AL	384.Ø	173.3	557.3	427.7	435.8	157.1	592.9
CL	479.6	233.2	712.8	521.6	532.Ø	214.6	746.6
FE	67Ø.7	363.4	1Ø34.1	7Ø7.5	717.8	337.7	1Ø55.5
CU	741.2	414.3	1155.5	775.7	784.7	385.2	1169.8
SN	1169.3	747.4	1916.7	1192.1	1179.5	687.5	1867.Ø
W	1599.2	1111Ø.4	2709.6	1607.6	1563.7	1Ø05.4	2569.2
PB	1744.9	1237.8	2982.7	1749.5	1692.Ø	1114.8	2806.9
U	1919.4	1392.8	3312.2	1920.Ø	1845.Ø	1247.Ø	3Ø91.9

SIGBAR = 35.Ø MB
C = 1.13 A**1/3 F
Ƶ = Ø.53 F
RØ = 1.3Ø F

MATERIAL	UNIFORM MODEL			WILLIAMS	WOOD-SAXON		
	SIGA	SIGD	SIGT	SIGA	SIGA	SIGD	SIGT
HE	83.3	22.9	1Ø6.2	119.9	1Ø6.3	14.8	121.Ø
LI	133.1	43.3	176.3	175.Ø	166.5	32.5	199.Ø
BE	163.6	57.2	22Ø.8	2Ø7.6	2Ø2.1	45.3	247.4
C	2Ø6.5	78.4	285.Ø	252.3	25Ø.8	65.3	316.1
N2	233.7	92.6	326.3	28Ø.2	28Ø.9	78.9	359.8
O2	259.9	1Ø6.9	366.8	3Ø6.9	3Ø9.5	92.6	4Ø2.1
F	297.7	128.3	425.9	344.9	35Ø.Ø	113.3	463.2
NE	3Ø9.9	135.4	445.3	357.2	362.9	12Ø.1	483.1
AL	391.4	185.2	576.4	438.3	447.6	168.Ø	615.6
CL	488.Ø	248.Ø	735.9	533.3	545.Ø	228.3	773.4
FE	68Ø.4	384.Ø	1Ø64.4	721.2	732.6	356.5	1Ø89.1
CU	751.2	437.Ø	1188.2	79Ø.2	8ØØ.Ø	4Ø5.6	1235.6
SN	1188.8	781.4	1962.2	1218.1	1197.4	716.3	1913.7
W	1611.6	1153.8	2765.3	1628.6	1583.6	1Ø4Ø.3	2623.9
PB	1757.4	1283.9	3Ø41.3	1771.5	1712.4	1151.5	2863.9
U	1932.1	1442.2	3374.2	1943.Ø	1866.Ø	1285.5	3151.5

SIGBAR = 37.0 MB
C = 1.13 A**1/3 F
Z = 0.53 F
R0 = 1.30 F

Table VI (cont'd)

MATERIAL	UNIFORM MODEL			WILLIAMS	WOOD-SAXON		
	SIGA	SIGD	SIGT	SIGA	SIGA	SIGD	SIGT
HE	85.8	24.8	110.6	124.7	110.8	16.2	127.0
LI	136.6	46.6	183.2	181.0	172.8	35.3	208.1
BE	167.6	61.5	229.1	214.0	209.2	49.1	258.3
C	211.2	84.0	295.3	259.5	258.9	70.4	329.4
N2	238.8	99.1	337.9	287.8	289.6	84.9	374.5
O2	265.3	114.2	379.4	314.8	318.6	99.4	418.1
F	303.5	136.7	440.2	353.4	359.8	121.2	481.0
NE	315.9	144.2	460.1	365.8	372.9	128.4	501.4
AL	398.1	196.3	594.4	447.8	458.7	178.7	637.4
CL	495.4	262.2	757.6	543.9	557.2	241.6	798.8
FE	688.9	403.7	1092.6	733.6	746.3	374.4	1120.7
CU	760.0	458.6	1218.6	803.2	814.2	425.0	1239.3
SN	1190.8	813.1	2003.9	1224.4	1214.0	743.1	1957.1
W	1622.2	1193.6	2815.8	1647.6	1601.9	1072.5	2674.4
PB	1768.1	1326.1	3094.3	1791.3	1731.3	1185.1	2916.4
U	1943.0	1486.9	3429.8	1963.8	1885.4	1320.7	3206.1

SIGBAR = 39.0 MB
C = 1.13 A**1/3 F
Z = 0.53 F
R0 = 1.30 F

MATERIAL	UNIFORM MODEL			WILLIAMS	WOOD-SAXON		
	SIGA	SIGD	SIGT	SIGA	SIGA	SIGD	SIGT
HE	88.1	26.7	114.9	129.1	115.2	17.6	132.8
LI	139.8	50.0	189.8	186.2	178.8	38.2	217.0
BE	171.4	65.7	237.1	219.8	216.0	52.9	268.9
C	215.5	89.5	305.1	265.9	266.7	75.5	342.2
N2	243.4	105.4	348.8	294.6	297.9	90.8	388.7
O2	270.2	121.3	391.5	321.9	327.4	106.1	433.5
F	308.8	144.9	453.7	360.9	369.0	129.0	498.1
NE	321.3	152.8	474.1	373.5	382.4	136.6	519.0
AL	424.2	207.3	611.5	456.4	469.2	189.1	658.3
CL	502.1	275.8	777.9	553.4	568.6	254.5	823.1
FE	696.4	422.4	1118.8	744.7	759.1	391.5	1150.6
CU	767.8	478.9	1246.7	814.8	827.5	443.5	1271.0
SN	1199.5	842.5	2042.0	1230.9	1229.3	768.1	1997.5
W	1631.3	1230.1	2861.4	1664.6	1618.9	1102.1	2721.0
PB	1777.4	1364.7	3142.1	1809.0	1748.7	1216.0	2964.8
U	1952.3	1527.7	3480.0	1982.4	1903.5	1353.0	3256.5

SIGBAR = 40.0 MB
C = 1.13 A**1/3 F
Z = 0.53 F
RO = 1.30 F

Table VI (cont'd)

MATERIAL	UNIFORM MODEL			WILLIAMS	WOOD-SAXON		
	SIGA	SIGD	SIGT	SIGA	SIGA	SIGD	SIGT
HE	89.3	27.7	117.0	131.0	117.3	18.3	135.7
LI	141.4	51.6	193.0	180.6	181.7	39.6	221.3
BE	173.1	67.8	241.0	222.4	219.3	54.8	274.1
C	217.6	92.3	309.8	268.8	270.4	78.1	348.5
N2	245.6	108.5	354.1	297.6	301.8	93.8	395.6
O2	272.5	124.8	397.3	325.1	331.5	109.5	441.0
F	311.3	149.0	460.2	364.4	373.5	132.9	506.4
NE	323.8	157.2	480.8	377.0	386.9	140.7	527.5
AL	407.0	212.6	619.6	460.3	474.2	194.2	668.4
CL	505.1	282.5	787.6	557.7	574.0	260.8	834.8
FE	699.9	431.4	1131.2	749.8	765.2	399.8	1165.0
CU	771.3	488.7	1260.1	820.1	833.8	452.4	1286.1
SN	1203.5	856.4	2059.9	1245.5	1236.6	780.0	2016.6
W	1635.4	1247.2	2882.7	1672.3	1626.9	1116.1	2743.0
PB	1781.5	1382.7	3164.2	1817.1	1757.0	1230.6	2987.6
U	1956.5	1546.7	3503.2	1990.9	1912.0	1368.1	3280.2

SIGBAR = 42.0 MB
C = 1.13 A**1/3 F
Z = 0.53 F
RO = 1.30 F

MATERIAL	UNIFORM MODEL			WILLIAMS	WOOD-SAXON		
	SIGA	SIGD	SIGT	SIGA	SIGA	SIGD	SIGT
HE	91.4	29.6	121.1	134.6	121.5	19.8	141.4
LI	144.3	54.9	199.3	193.0	187.4	42.5	229.9
BE	176.5	72.0	248.5	227.2	225.7	58.6	284.3
C	221.4	97.7	319.0	274.1	277.7	83.2	360.8
N2	249.7	114.7	364.3	303.2	309.5	99.6	409.1
O2	276.8	131.6	408.5	330.9	339.6	116.1	455.6
F	315.9	156.9	472.8	378.6	388.1	140.5	522.6
NE	328.5	165.2	493.7	383.3	395.6	148.6	544.2
AL	412.2	223.4	635.2	467.3	483.7	204.2	687.9
CL	510.8	295.3	806.1	565.5	584.3	273.0	857.3
FE	706.2	448.6	1154.8	758.9	776.8	415.7	1192.5
CU	777.8	507.5	1285.3	829.7	845.8	469.4	1315.2
SN	1210.6	892.8	2093.4	1257.4	1250.5	802.6	2053.1
W	1642.8	1279.3	2922.2	1686.2	1642.3	1142.5	2784.7
PB	1789.8	1416.4	3205.4	1831.6	1772.8	1258.2	3030.8
U	1964.9	1582.1	3546.1	2006.1	1928.3	1396.6	3325.0

SIGBAR = 44.0 MB
C = 1.13 A**1/3 F
Z = 0.53 F
RØ = 1.30 F

Table VI (cont'd)

MATERIAL	UNIFORM MODEL SIGA	SIGD	SIGT	WILLIAMS SIGA	WOOD-SAXON SIGA	SIGD	SIGT
HE	93.5	31.5	125.0	137.6	125.6	21.3	147.0
LI	147.1	58.2	205.3	196.7	192.9	45.4	238.3
BE	179.6	76.1	255.7	231.2	231.9	62.4	294.3
C	224.9	102.9	327.8	278.6	284.6	88.2	372.8
N2	253.4	120.7	374.1	307.9	316.8	105.4	422.2
O2	280.8	138.3	419.1	335.9	347.3	122.5	469.8
F	320.1	164.6	484.6	375.8	390.2	148.0	539.2
NE	332.8	173.2	506.0	388.7	403.9	156.4	560.3
AL	416.9	233.0	650.0	473.3	492.7	214.0	706.7
CL	515.9	307.6	823.5	572.1	594.1	284.8	878.9
FE	711.8	464.9	1176.8	766.7	787.7	430.8	1218.6
CU	783.6	525.1	1308.8	837.8	857.0	485.7	1342.7
SN	1216.9	907.3	2124.2	1267.5	1263.5	823.8	2087.2
W	1649.3	1308.8	2958.1	1698.1	1656.7	1166.9	2823.6
PB	1795.5	1447.2	3242.7	1844.0	1787.7	1283.3	3071.0
U	1970.6	1614.4	3585.0	2019.1	1943.7	1422.9	3366.6

SIGBAR = 46.0 MB
C = 1.13 A**1/3 F
Z = 0.53 F
RØ = 1.30 F

MATERIAL	UNIFORM MODEL SIGA	SIGD	SIGT	WILLIAMS SIGA	WOOD-SAXON SIGA	SIGD	SIGT
HE	95.4	33.5	128.8	140.1	129.6	22.9	152.5
LI	149.7	61.4	211.1	199.7	198.2	48.4	246.6
BE	182.4	80.2	262.6	234.6	237.8	66.2	304.0
C	228.2	108.1	336.3	282.3	291.2	93.2	384.4
N2	256.9	126.5	383.4	311.8	323.8	111.1	435.0
O2	284.4	144.8	429.3	340.0	354.6	128.9	483.5
F	323.9	172.0	495.9	380.2	397.9	155.3	553.2
NE	336.7	181.0	517.7	393.1	411.7	164.0	575.7
AL	421.2	242.7	663.9	478.2	501.3	223.4	724.7
CL	520.5	319.3	839.9	577.6	603.3	296.1	899.5
FE	716.9	480.4	1197.3	773.1	798.0	445.3	1243.3
CU	788.8	541.8	1330.6	844.6	867.6	501.1	1368.7
SN	1222.4	930.0	2152.4	1276.0	1275.7	843.6	2119.3
W	1655.3	1335.8	2992.8	1707.9	1670.2	1189.6	2859.9
PB	1801.2	1475.4	3276.7	1854.3	1801.6	1336.8	3138.4
U	1976.3	1643.8	3622.2	2029.9	1953.1	1447.3	3405.4

SIGBAR = 40.0 MB
C = 1.13 A**1/3 F
Z = 0.53 F
RØ = 1.30 F

Table VI (cont'd)

MATERIAL	UNIFORM MODEL			WILLIAMS	WOOD-SAXON		
	SIGA	SIGD	SIGT	SIGA	SIGA	SIGD	SIGT
HE	97.2	35.4	132.6	142.1	133.5	24.4	157.9
LI	152.0	64.6	216.7	202.2	233.3	51.3	254.6
BE	185.1	84.1	269.2	237.2	243.5	70.0	313.5
C	231.2	113.1	344.3	285.2	297.6	98.1	395.7
N2	260.0	132.2	392.3	315.0	330.5	116.8	447.3
O2	287.7	151.2	438.9	343.3	361.6	135.2	496.8
F	327.5	179.2	506.7	383.7	405.3	162.5	567.8
NE	340.3	188.5	528.7	396.7	419.2	171.5	590.7
AL	425.1	252.0	677.1	482.2	509.4	232.6	742.0
CL	524.7	330.5	855.2	582.0	612.1	307.1	919.2
FE	721.4	495.0	1216.4	778.2	807.7	459.1	1266.8
CU	793.4	557.5	1350.9	849.9	877.7	515.7	1393.4
SN	1227.3	951.1	2178.4	1282.6	1287.3	862.2	2149.5
W	1660.1	1360.6	3020.7	1715.7	1683.1	1210.8	2893.9
PB	1806.3	1531.2	3337.5	1862.5	1814.9	1328.7	3143.6
U	1981.4	1670.7	3652.1	2038.5	1971.8	1469.9	3441.7

SIGBAR = 50.0 MB
C = 1.13 A**1/3 F
Z = 0.53 F
RØ = 1.30 F

MATERIAL	UNIFORM MODEL			WILLIAMS	WOOD-SAXON		
	SIGA	SIGD	SIGT	SIGA	SIGA	SIGD	SIGT
HE	98.9	37.2	136.1	143.6	137.3	26.0	163.2
LI	154.3	67.8	222.0	204.0	208.3	54.2	262.5
BE	187.6	88.2	275.6	239.2	249.0	73.7	322.7
C	233.9	118.0	352.0	287.4	303.6	123.0	406.7
N2	263.0	137.8	400.8	317.3	336.9	122.3	459.3
O2	290.8	157.3	448.1	345.7	368.3	141.4	509.7
F	330.7	186.2	516.9	386.2	412.3	169.5	581.8
NE	343.5	195.7	539.3	399.3	426.3	178.8	605.1
AL	428.6	262.9	689.5	485.1	517.2	241.5	758.7
CL	528.5	341.2	869.7	585.2	620.4	317.6	938.0
FE	725.5	508.8	1234.2	782.0	817.0	472.2	1289.2
CU	797.5	572.3	1369.8	853.9	887.2	529.6	1416.8
SN	1231.7	970.6	2202.3	1287.6	1298.3	879.6	2177.9
W	1664.5	1383.4	3047.9	1721.5	1695.3	1230.6	2925.9
PB	1810.8	1524.9	3335.6	1868.5	1827.4	1349.1	3176.5
U	1985.9	1695.2	3681.1	2044.8	1984.8	1491.0	3475.7

LIST OF REFERENCES

1. See, for example, Muirehead, The Physics of Elementary Particles, Pergamon Press, Oxford (1965).
2. A. Berthon, J. Vrana, I. Butterworth, P. J. Lilchfield, J. R. Smith, J. Meyer, E. Pauli and B. Tallini, Nucl. Phys. B24, 417 (1970).
3. C. W. Akerlof, P. K. Caldwell, C. T. Coffin, P. Kalbaci, D. I. Meyer, P. Schmüeser and K. C. Stanfield (To be published in Phys. Rev. Lett.) 1971.
4. V. D. Barger and D. B. Cline, Phenomenological Theory of High Energy Scattering, W. A. Benjamin, Inc. 1969.
5. See, for example, C. T. Coffin, N. Dikmen, L. Ettlinger, D. Meyer, A. Saulys, K. Terwilliger Phys. Rev. 159, 1169 (1967).
6. Many references can be found in the paper by V. D. Barger and R.J. Philips, Phys. Rev. 187, 2210 (1969).
7. P. Sonderegger, J. Kirz, O. Guisan, P. Falk-Vairant, C. Bruneton, P. Borgead, A. V. Stirling, Phys. Letters 20, 75 (1966).
8. A. V. Stirling, P. Sonderegger, J. Kirz, P. Falk-Vairant, O. Guisan, C. Bruneton, P. Borgeand, M. Yuert, J. P. Guilland, C. Caverzasio and B. Amblard, Phys. Rev. Lett. 14, 763 (1965).
9. M. A. Wahling and I. Manneli, Phys. Rev. 168, 1515 (1968).
10. S. M. Pruss, C. W. Akerlof, D. I. Meyer, S. P. Ying,

J. Lales, R. A. Lundy, D. R. Rust, C. E. W. Ward and D. D. Yovanovitch, Phys. Rev. Lett. 23, 189 (1969).

11. K. S. Han, C. W. Akerlof, P. Schmüeser, P. N. Kirk, D. R. Rust, C. E. W. Ward, D. D. Yovanovitch and S. M. Pruss, Phys. Rev. Lett. 24, 1353 (1970).
12. A. Bashian, G. Finocchiaro, M. L. Good, P. D. Grannis, O. Guisan, J. Kirz, Y. Y. Lee, R. Pittman, G. C. Fischer and D. D. Reeder (To be published in Phys. Rev.) 1971.
13. S. P. Ying, C.W. Akerlof, D.I.Meyer, S.M.Pruss, J.Lales, R.A.Lundy, D.R.Rust, C.E.W.Ward and D.D.Yovanovich, Phys. Letters, 30B, 289(1969)
14. W. S. C. Williams, An Introduction to Elementary Particles, 1971, Academic Press.
15. W. A. Wenzel, IEEE Trans. on Nucl. Science 34 (June 1966).
16. W. Baker, Phys. Today, 41 (July 1967).
17. V. Perez-Mendez and J. M. Pfab, Nucl. Inst. and Meth. 33, 141 (1965).
18. F. A. Kirsten, K. L. Lee and J. Conragan, IEEE Trans. on Nucl. Science 583 (June 1966).
19. "Remendur" is an alloy of 49% iron, 49% cobalt and 2% vanadium manufactured by Wilber B. Driver Company, Newark, New Jersey.
20. Private communication, Dr. D. Yovanovitch, Argonne National Laboratory.
21. G. Kallen, Elementary Particle Physics, 1964, Addison-Wesley.

22. H. Pilkuhn, The Interaction of Hadrons, 1967, North-Holland Publishing Company, Amsterdam.

23. N. Schmitz, High Energy Reactions, 1970, Max-Planck Institut für Physik und Astrophysik, München.

24. D. D. Reeder and K. V. L. Sarma, Phys. Rev. 172, 1566 (1968).

25. K. V. L. Sarma and D. D. Reeder, Nuovo Cimento, L III A, 808 (1968).

26. W. R. Butler, UCRL-19845 (1970).

27. M. Aderholz, M. Deutschmann, E. Keppel, G. Kraus, H. Weber, U. Gensch, G. Grote, S. Nowak, D. Pose, H. Böttcher, T. A. Byer, V. T. Cocconi, E. Flaminio, J. D. Hansen, G. Kellner, U. Kruse, J. Loskiewicz, M. Markytan, D. R. O. Morrison, N. C. Barford, D. P. Dallman, S. J. Goldsack, N. C. Mukherjee, W. Kittel, C. Kraft, D. Kuhn, G. Otter and I. Wacek, Nucl. Phys. B7, 111 (1968).

28. L. Stodolsky and J. J. Sakurai, Phys. Rev. Lett. 11, 90 (1963).

29. J. J. Sakurai, Advanced Quantum Mechanics, Addison-Wesley (1967).

30. R. H. Dalitz and D. R. Yennie, Phys. Rev. 105, 1598 (1957).

31. L. Stodolsky, Phys. Rev. 134, B1099 (1964).

32. W. S. McDonald, V. Z. Peterson, D. R. Corson, Phys. Rev. 107, 577 (1957).

33. G. F. Chew and F. E. Low, Phys. Rev. 101, 1579 (1956).

34. G. F. Chew and F. E. Low, Phys. Rev. 106, 1345 (1957).

35. S. Fubini, Y. Nambu and V. Wataghin, Phys. Rev. 111, 329 (1958).

36. G. Gidal, G. Borreani, D. Grether, F. Lott, R. W. Birge, S. Y. Fung, W. Jackson and R. Poe, Phys. Rev. Lett. 23, 994 (1969).

37. Y. Goldschmidt-Clermont, V. P. Henri, B. Jongejans, A. Moisseeu, F. Muller, J. M. Perreau, A. Prokes, Y. Yarba, W. DeBaere, J. Debaisieux, P. Dufour, F. Grard, J. Heughebaert, L. Pope, P. Reeters, F. Verbeure and R. Windmolders, Nuovo Cimento 46A, 539 (1966).

38. M. Gell-Mann, Phys. Rev. 125 1067 (1962).

39. Y. Ne'eman, Nucl. Phys. 26 222 (1961).

40. S. H. Glashow, Nuovo Cimento 25 337 (1962).

41. S. H. Glashow, Nuovo Cimento 26, 662 (1962).

42. R. E. Behrends et al., Rev. Mod. Phys. 34, 1 (1962).

43. D. Birmbaum, R. M. Edelstein, N. C. Hien, T. J. McMahon, J. F. Mucci, J. S. Russ, E. W. Anderson, E. J. Beleser, H. R. Blieden, G. B. Collins, D. Garelick, J. Menes and F. Turkot, Phys. Letters 31B, 484 (1970).

44. G. R. Renninger and K. V. L. Sarma, Phys. Rev. 2, 1281 (1970).

45. C. R. Renninger and K. V. L. Sarma, Phys. Rev. 178, 2201 (1969).

46. J. W. Cronin, R. Cool and A. Abashian, Phys. Rev. 107, 1121 (1957).

47. R. J. Abrams, R. L. Cool, G. Giacomelli, T. F. Kycia, B. A. Leontic, K. K. Li, A. Lundly, D. N. Michael and J. Teiger (To be published) 1970.

48. M. J. Longo and Burton J. Moyer, Phys. Rev. 125, 701 (1962).

49. A. Ashmore, G. Cocconi, A. N. Diddens and A. M. Wetherell, Phys. Rev. Lett. 5, 576 (1960).

50. R. W. Williams, Rev. Mod. Phys. 36, 815 (1964).

51. R.G.Glauber, Lectures in Theoretical Physics,p315, Interscience Publisher, New York, 1959.